Draft version August 17, 2023
Typeset using LaTeX twocolumn style in AASTeX631

Bioverse: The Habitable Zone Inner Edge Discontinuity as an Imprint of Runaway Greenhouse Climates on Exoplanet Demographics

Martin Schlecker,[1] Dániel Apai,[1,2] Tim Lichtenberg,[3] Galen Bergsten,[2] Arnaud Salvador,[2] and Kevin K. Hardegree-Ullman[1]

[1]Steward Observatory, The University of Arizona, Tucson, AZ 85721, USA; schlecker@arizona.edu
[2]Lunar and Planetary Laboratory, The University of Arizona, Tucson, AZ 85721, USA
[3]Kapteyn Astronomical Institute, University of Groningen, PO Box 800, 9700 AV Groningen, The Netherlands

ABSTRACT

Long-term magma ocean phases on rocky exoplanets orbiting closer to their star than the runaway greenhouse threshold – the inner edge of the classical habitable zone – may offer insights into the physical and chemical processes that distinguish potentially habitable worlds from others. Thermal stratification of runaway planets is expected to significantly inflate their atmospheres, potentially providing observational access to the runaway greenhouse transition in the form of a "habitable zone inner edge discontinuity" in radius–density space. Here, we use `Bioverse`, a statistical framework combining contextual information from the overall planet population with a survey simulator, to assess the ability of ground- and space-based telescopes to test this hypothesis.

We find that the demographic imprint of the runaway greenhouse transition is likely detectable with high-precision transit photometry for sample sizes $\gtrsim 100$ planets if at least $\sim$10 % of those orbiting closer than the habitable zone inner edge harbor runaway climates. Our survey simulations suggest that in the near future, ESA's *PLATO* mission will be the most promising survey to probe the habitable zone inner edge discontinuity. We determine survey strategies that maximize the diagnostic power of the obtained data and identify as key mission design drivers: 1. A follow-up campaign of planetary mass measurements and 2. The fraction of low-mass stars in the target sample. Observational constraints on the runaway greenhouse transition will provide crucial insights into the distribution of atmospheric volatiles among rocky exoplanets, which may help to identify the nearest potentially habitable worlds.

1. INTRODUCTION

Despite recent advancements in observational techniques, our understanding of terrestrial-sized planets remains woefully limited, with fundamental aspects of their nature, composition, and potential habitability still largely unknown. Due to the inherent biases of current exoplanet detection techniques, the best-studied category of rocky exoplanets at present is that of hot or warm, close-in planets (Jontof-Hutter 2019; Bean et al. 2021). These experience thermal states that are in some aspects comparable to the ones of the inner solar system bodies at early stages of their evolution (Ikoma et al. 2018; Chao et al. 2021), which likely profoundly affected the distribution of volatiles between planetary core, mantle, and atmosphere. Studying the geophysical state of hot exoplanets can thus inform our understanding of the early evolutionary stages of Earth and other habitable worlds (Lichtenberg et al. 2022; Krijt et al. 2022).

An example from the solar system for the potential significance of these early stages are the divergent atmospheric evolutions of Venus and Earth (e.g., Kane et al. 2019, 2021; Salvador et al. 2023). While having accreted from a similar mass reservoir (Raymond et al. 2020; Kleine et al. 2020; Mezger et al. 2020; Zahnle & Carlson 2020) and despite their similar bulk properties (Smrekar et al. 2018), they evolved into planets with very different surface conditions (Donahue et al. 1982; Kasting 1988; Hamano et al. 2013; Kane et al. 2014; Way & Del Genio 2020; Turbet et al. 2021). Both planets likely underwent a giant impact phase (Raymond et al. 2020; Gillmann et al. 2020; Liu et al. 2022) that melted their mantles (Elkins-Tanton 2012; Schaefer & Elkins-Tanton 2018; Lichtenberg et al. 2022). Magma ocean states play a substantial role in establishing the long-term geophysical and climatic regimes of rocky planets (Fegley et al. 2020), in particular owing to efficient heat and volatile transfers between interior and atmosphere in the absence of a stiff boundary separating them (Kite & Schaefer 2021; Dorn & Lichtenberg 2021; Salvador et al. 2023). Due to these similar formation sequences, it was commonly assumed that the divergence of Venus and Earth

– in particular Venus' water loss – occurred late in their evolution (e.g., Way & Del Genio 2020).

Yet, Hamano et al. (2013) suggested that the present-day dry conditions on Venus may have been directly inherited from the early magma ocean stage. If a strongly infrared-absorbing, condensable species such as water was dominant in the atmosphere, the resulting strong thermal blanketing effect would prevent the planet to efficiently radiate to space and maintain the surface molten (Ingersoll 1969; Kasting 1988; Pierrehumbert 2010; Goldblatt et al. 2013; Leconte et al. 2015; Salvador et al. 2017). This runaway greenhouse state can extend the magma ocean stage to hundreds of Myr (Schaefer et al. 2016; Barth et al. 2021), enough to remove the entire water reservoir from a rocky planet by H_2O photolysis and subsequent hydrodynamic escape of hydrogen (Wordsworth & Pierrehumbert 2013, 2014; Luger & Barnes 2015). For Venus, the atmospheric composition (Gillmann et al. 2020) and comprehensive analysis of meteoritic samples across the Solar System (Alexander et al. 2018; Broadley et al. 2022) suggest that it went through this phase. Although the past presence or absence of a Venusian water ocean has not been definitely established (Raymond et al. 2006, 2007; Hamano et al. 2013; Way et al. 2016; Kane et al. 2019, 2021; Turbet et al. 2021; Warren & Kite 2023), a transient habitable phase cannot be conclusively ruled out (e.g., Way et al. 2016; Salvador et al. 2017; Krissansen-Totton et al. 2021).

The runaway greenhouse transition is a robust prediction from climate models (Kasting 1988; Nakajima et al. 1992; Goldblatt & Watson 2012; Forget & Leconte 2014; Boukrouche et al. 2021; Chaverot et al. 2022), and its impact on planetary bulk properties has been shown to be in the detectable range of current astronomical instrumentation (Goldblatt 2015). In particular, planets in a runaway greenhouse state are expected to be thermally inflated (Turbet et al. 2019, 2020; Mousis et al. 2020), which directly increases their transit radii by an amount that is a function of the water content. However, dissolution of water (e.g., Elkins-Tanton & Seager 2008; Hier-Majumder & Hirschmann 2017; Salvador & Samuel 2023) in the magma may decrease this effect (Dorn & Lichtenberg 2021), and chemical exchange between core and mantle material may influence the amount and speciation of outgassed volatiles that are visible in the atmosphere via transmission spectroscopy (Lichtenberg 2021; Schlichting & Young 2022). Astronomical observations of planets that are currently in a runaway greenhouse state may thus constrain properties of their mantles and establish an observational connection between exoplanetary interiors and atmospheres (Lichtenberg et al. 2022; Wordsworth & Kreidberg 2022).

Of particular relevance is that the radiation-induced transition between a runaway greenhouse state and a temperate climate is thought to occur at a relatively sharp instellation threshold (Goldblatt et al. 2013; Leconte et al. 2013a; Kopparapu et al. 2013). Consequently, the instellation at which the runaway greenhouse transition occurs is aptly considered to be the inner boundary of the habitable zone (e.g., Ramirez 2018; Salvador et al. 2023). Its prevalent definition refers to the possibility of a sustained liquid water body on the surface of an Earth-like planet with an oxidized $CO_2/H_2O/N_2$-rich atmosphere (Kasting et al. 1993; Kopparapu et al. 2013, 2014); its exact spatial location and extent may be strongly influenced by the interior and atmosphere oxidation state and resulting atmosphere composition (Pierrehumbert & Gaidos 2011; Ramirez & Kaltenegger 2017, 2018; Katyal et al. 2019; Graham & Pierrehumbert 2020; Graham et al. 2022; Hakim et al. 2023). The fundamental concept of a habitable zone dates back centuries (Newton 1687; Whewell 1858; Shapley 1953; Huang 1959), and its modern form has proven popular in the planetary literature[1]. However, it should be emphasized that the habitable zone, as it stands today, is merely a concept based on theoretical predictions and geochemical evidence from one planet – Earth (Catling & Zahnle 2020) – and its general validity remains controversial (e.g., Cockell et al. 2016; Moore et al. 2017; Tuchow & Wright 2023). The question naturally emerges if a planetary habitable zone – in its common form with boundaries defined by stellar irradiation – is a predictive theoretical concept and how the habitable zone hypothesis can be tested observationally.

Observational tests being considered include searches for direct evidence of liquid water conveyed by ocean glint (Williams & Gaidos 2008; Robinson et al. 2010; Lustig-Yaeger et al. 2018) or water vapor in planetary atmospheres (Suissa et al. 2020). A different approach relies on comparative planetology: aiming for a statistical detection in a planet population provides robustness against ambiguity that could otherwise arise from individual variations in a planet's composition or geophysical history (Checlair et al. 2019; Apai et al. 2019b). Tests suggested in the literature include determining, for a range of orbital distances, atmospheric H_2O and CO_2 abundances, planetary albedos (Bean et al. 2017;

[1] At the time of writing, a search of the term "habitable zone" in the titles and abstracts of refereed articles in the National Aeronautics and Space Administration (NASA) Astrophysics Data System returned ~ 1700 results.

Bixel & Apai 2021), or colors (Crow et al. 2011; Bixel & Apai 2020), or testing the relationship between CO_2 partial pressure and incident flux (Lehmer et al. 2020). All these tests require surveying a large enough sample of terrestrial-sized planets with next-generation instruments, rendering them out of reach in the immediate future.

Here, we explore the feasibility of a statistical test of the habitable zone hypothesis by surveying planetary bulk properties close to its inner edge, the runaway greenhouse transition. Our goal is to assess the ability of near-future transit surveys to test the hypothesis that the runaway greenhouse effect causes a discontinuity of planetary radii and bulk densities when ordered by receiving instellation (Turbet et al. 2019). Our main tool for this is `Bioverse`, a simulation framework for assessing the statistical power of exoplanet surveys (Bixel & Apai 2021). It consists of a sample generator that populates stars from the *Gaia* catalog (Hardegree-Ullman et al. 2023; Prusti et al. 2016; Gaia Collaboration et al. 2022a) with planetary systems based on state-of-the-art occurrence rates (Bergsten et al. 2022), a flexible survey simulator that allows for a broad range of trade studies, and a hypothesis testing module that quantifies the survey's ability to detect a previously injected trend. Trying different instrumentation and survey designs, we use `Bioverse` to recover runaway greenhouse-induced effects based on model predictions (Turbet et al. 2020; Dorn & Lichtenberg 2021) that we inject into a baseline planet population.

In particular, we test the capability of the *PLATO* (PLAnetary Transits and Oscillation of stars, Rauer et al. 2016) mission, which will measure the radii of a large number of terrestrial-sized planets, to detect the radius/density discontinuity and determine its sensitivity to model assumptions and fundamental processes. We then perform a parameter study to explore which trades in the survey design of a *PLATO*-like mission maximize its diagnostic power to test runaway greenhouse climate models through the detection of the habitable zone inner edge discontinuity.

We organize the paper as follows: Section 2 introduces the baseline model we use to produce synthetic star and planet samples. In Section 3, we describe the model component that produces runaway greenhouse-induced transit radius changes. Section 4 explains our survey simulations and hypothesis tests. We present our results in Section 5 before interpreting them in Section 6. Finally, we summarize our findings in Section 7.

2. BASELINE MODEL

The goal of this study is to determine – for different configurations of near-future exoplanet surveys – the confidence level with which the runaway greenhouse threshold can be detected statistically. Our basic methodology was as follows: We expanded the `Bioverse` framework (Bixel & Apai 2020, 2021)[2] to generate synthetic samples of stars that host planets according to the observed exoplanet demographics. We then adapted planetary bulk properties as predicted from models of runaway greenhouse atmospheres, simulated observations of the planets, and computed Bayesian evidences in favor of a habitable zone inner edge discontinuity (see diagram in Figure 1). In this section, we review the source of the stellar sample, the modeled luminosity evolution, the generation of a synthetic planet sample, and the orbital parameters of the planets. An overview of our key assumptions and model parameters can be found in Table 1.

2.1. *Stellar sample from Gaia DR3*

The original `Bioverse` stellar catalog was generated randomly from the Chabrier (2003) stellar mass function. Improved parallax and photometric data from the *Gaia* mission made it possible to generate a homogeneous and complete stellar catalog out to about 100 pc, which became the new standard stellar catalog for `Bioverse` (Hardegree-Ullman et al. 2023). Here, we briefly describe how we derived the stellar effective temperature $T_{\rm eff}$, luminosity $L_\star$, stellar radius $R_\star$, and stellar mass $M_\star$.

Hardegree-Ullman et al. (2023) used the *Gaia* Catalogue of Nearby Stars (hereafter GCNS, Smart et al. 2021) as the basis for deriving stellar parameters for the `Bioverse` catalog. The GCNS identified stars out to 120 pc and includes *Gaia* DR3 parallaxes and photometry in G, G_{BP}, and G_{RP} bands (Gaia Collaboration et al. 2022b) and K_S band photometry from 2MASS (Cutri et al. 2003), all of which were used in stellar classification. From this information, we computed colors and absolute magnitudes and applied initial color-magnitude cuts to remove non-main sequence stars. We derived effective temperatures primarily from color-temperature relations derived using the main sequence stellar parameters table from Pecaut & Mamajek (2013). Luminosities were computed from absolute G-band mag-

[2] `Bioverse` is actively maintained and documented open source software written in Python. Its latest version and documentation can be found at https://github.com/danielapai/bioverse.

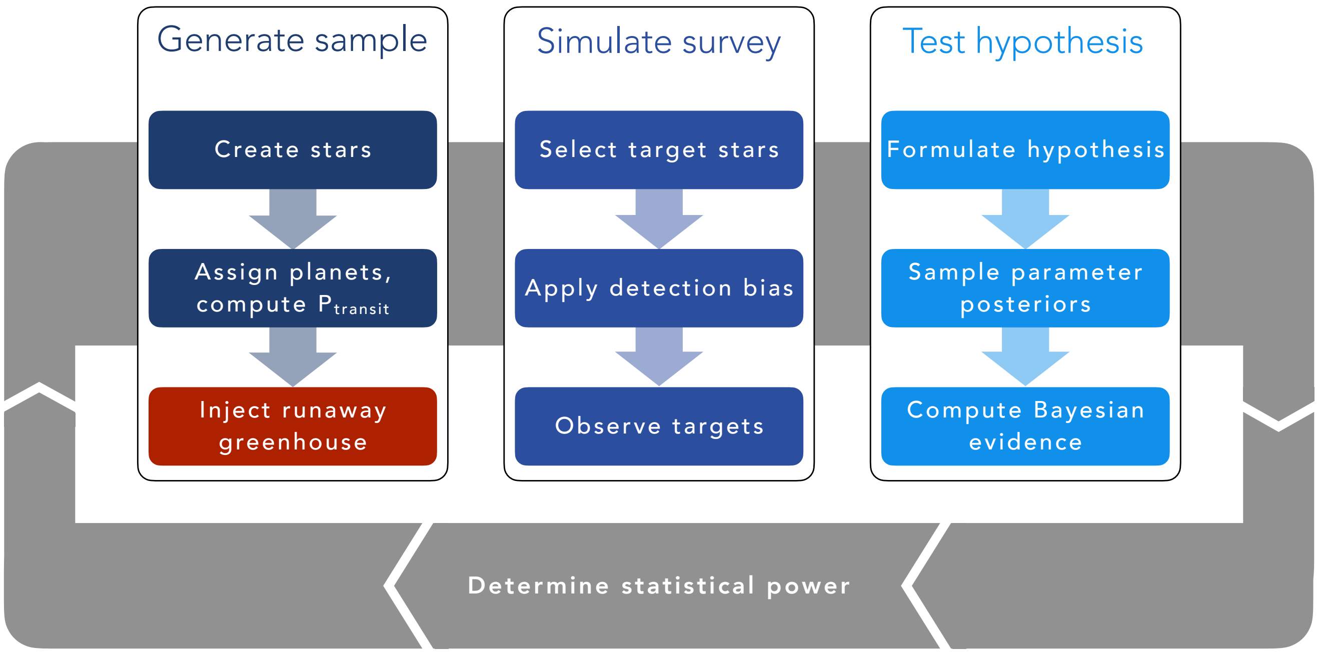

Figure 1. Workflow of our hypothesis testing with `Bioverse`. First, we generate a sample of stars and populate them with planets based on *Kepler* demographics. A fraction of them are then assigned a runaway greenhouse climate based on the model described in Sect. 3. We then simulate an exoplanet survey, whereby selection effects and detection biases are introduced. Finally, we test the runaway greenhouse hypothesis based on data from the survey simulation. By iterating through these steps, we compute the statistical power of testing the hypothesis for different survey designs.

nitudes and a derived bolometric correction. We computed stellar radii with the effective temperatures and luminosities using the Stefan-Boltzmann law or using absolute K_S-band magnitudes and an empirical radius-luminosity relation from Mann et al. (2015) for targets within the absolute magnitude range of M dwarfs. Finally, we derived masses from the mass-luminosity relation of Torres et al. (2010) for stars with $M_\star \gtrsim 0.7\,M_\odot$, and from that of Mann et al. (2019) for targets within the absolute magnitude range of M dwarfs. The derived stellar parameters were compared to measured parameters for all known exoplanet hosts from the literature and were found to be consistent within 1%, 3%, and 5.5% for $T_{\rm eff}$, $R_\star$, and $M_\star$, respectively, which are all below the typical measurement uncertainties of 3.3%, 6.8%, and 7.9%, respectively (Hardegree-Ullman et al. 2023). From this catalog, `Bioverse` samples stars within an isotropic distance from the solar system as required by the planetary sample size.

2.2. *Stellar luminosity evolution*

Planetary systems are hosted by stars of a wide range of ages, and stellar luminosities evolve with time. Since the occurrence of a runaway greenhouse state is highly dependent on the amount of radiation received by the planet, and thus on the luminosity of the host star, we assigned age-dependent luminosities to our synthetic stars.

While stellar ages are notoriously poorly constrained (e.g., Adams et al. 2005), the age distribution of planet host stars in the Solar neighborhood was shown to be broadly consistent with uniform (Reid et al. 2007; Gaidos et al. 2023). For our synthetic stars, we thus drew random ages from a uniform distribution from 0 Gyr to 10 Gyr. We then assigned each star a luminosity from the mass-dependent evolutionary models of Baraffe et al. (1998). Figure 2 shows the corresponding luminosity evolution as a function of stellar mass and age.

2.3. *Synthetic planet sample*

Next, we assigned to the stellar sample planetary systems with frequencies, orbital parameters, and bulk properties derived from the *Kepler* mission. We adopted the model from Bergsten et al. (2022), which defines the occurrence rate of small planets in radius and orbital period. Following Youdin (2011), their inferred occurrence

Table 1. Key assumptions and model parameters used in our simulation setup

Parameter	Value	Unit	Description
Stellar sample			
$G_{\rm max}$	16		Maximum Gaia magnitude
$M_{\star,\rm max}$	1.5	$M_\odot$	Maximum stellar mass
Luminosity evolution			Baraffe et al. (1998)
Planetary parameters			
$M_{\rm P}$	0.1 – 2.0	$\rm M_\oplus$	Planetary mass range
$R_{\rm P,min}$	0.75	$R_\oplus$	Minimum planet radius
Baseline mass-radius relation			Zeng et al. (2016) 100 % $MgSiO_3$ [a]
$\delta_{\rm min}$	80	ppm	Minimum transit depth
$P_{\rm max}$	500	d	Maximum orbital period [d]
S	10 – 2000	$\rm W\,m^{-2}$	Net instellation range
$S_{\rm thresh}$	280	$\rm W\,m^{-2}$	Threshold instellation for runaway greenhouse
Runaway greenhouse model			
Runaway greenhouse atmospheric models			Turbet et al. (2020); Dorn & Lichtenberg (2021)
x_{H_2O}	10^{-5}–0.1		Bulk water mass fraction (fiducial case: 0.005)
$f_{\rm rgh}$	0–1		Dilution factor (fiducial case: 0.8)
Priors			
$\Pi(S_{\rm thresh})$	[10, 1000]	$\rm W\,m^{-2}$	uniform
$\Pi(x_{H_2O})$	[10^{-5}, 0.1]		log-uniform
$\Pi(f_{\rm rgh})$	[0, 1]		uniform
$\Pi(\langle R_{\rm P}\rangle_{\rm out})$	[0, 15]	$R_\oplus$	Mean radius of non-runaway planets, uniform

[a] For a comparison with alternative interior compositions, see Appendix A.3.

rate density can be expressed in the form

$$\frac{\mathrm{d}^2 n}{\mathrm{d}R\,\partial P} = F_0 C_n g(R, P, M_\star), \tag{1}$$

where F_0 represents the average number of planets per star, C_n is a normalization constant, and the shape function $g(R, P, M_\star)$ describes the distribution of planets in radius, orbital period, and stellar host mass. `Bioverse` generates planets based on the above occurrence rate density and assigns them to the previously generated stars.

2.4. *Orbit parameters and planet masses*

Eccentric orbits alter the probability of a planet to transit (e.g., Barnes 2007). The distribution of eccentricities e of exoplanets has been found to resemble a Beta function (Kipping 2013), which we chose to draw synthetic eccentricities from. Following Kipping (2013), we used a Beta distribution with parameters $a = 0.867$ and $b = 3.03$, and truncated the distribution at $e = 0.8$. Assuming isotropic alignments of orbits, we assigned each planet an inclination drawn from a distribution uniform in $\cos(i)$.

To assign masses to our planets, we use the semi-empirical mass-radius relationship assuming a pure $MgSiO_3$ composition from Zeng et al. (2016) (see green line in Figure 3). This represents the baseline bulk density before any climate-related effects are applied.

2.5. *Transit probability*

We model the occurrence of transits by assuming isotropic orientations of planetary orbits and calculating the impact parameters $b = a\cos(i)/R_\star$. Following the approach in Bixel & Apai (2021), we further consider only planets with $|b| < 1$. For these cases we calculate the transit depth

$$\delta = \left(\frac{R_{\rm P}}{R_\star}\right)^2, \tag{2}$$

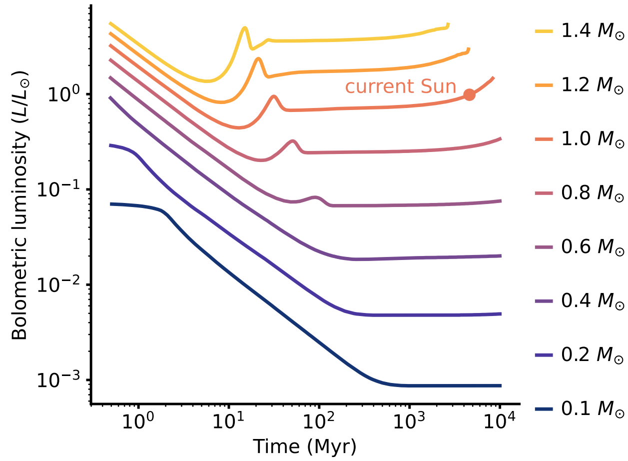

Figure 2. Bolometric luminosity tracks of stars with different masses, computed from stellar evolution models of Baraffe et al. (1998). Low-mass stars, which make up the majority of stars in the solar neighborhood, undergo an extended early phase of several magnitudes higher luminosity before entering a lifetime of relative faintness.

which is relevant for the detection probability of the respective planet (see Sect. 4.1). Excluding all non-transiting planets diminishes the sample to 1.5 % of its original size.

3. RUNAWAY GREENHOUSE MODEL

The climate state of a planet has a direct influence on its apparent size measured by transit photometry (Turbet et al. 2019, 2020; Mousis et al. 2020; Aguichine et al. 2021). With even a fraction of the Earth's water inventory, a planet absorbing more flux than the radiation limit of steam atmospheres was found to enter a runaway greenhouse state resulting in a global magma ocean (Lichtenberg et al. 2021; Boukrouche et al. 2021, but see Selsis et al. (2023) for a contrasting viewpoint). We use predictions on transit atmospheric thickness from geophysical models to derive the change in transit radius and bulk density that planets with instellation-induced runaway greenhouse climates experience, depending on the distribution of water between planetary interior and atmosphere, and on the resulting thermal atmospheric structure (Dorn & Lichtenberg 2021; Salvador & Samuel 2023).

The net absorbed stellar fluxes of planets are a function of intrinsic atmospheric properties such as their albedo, which are generally poorly constrained for planets outside the solar system (e.g., Angerhausen et al. 2015; Parmentier & Crossfield 2018; Mansfield et al. 2019). For instance, a planet with a high albedo may sustain temperate conditions closer to the star than the same planet with a lower albedo and located further away from the star. Here, we assume global redistribution of incoming flux and a fixed Bond albedo of 0.3, comparable to Earth's (Haar & Suomi 1971). We do not take into account additional heating sources such as tidal effects (e.g., Barnes et al. 2013).

While we search for the signature of runaway greenhouse climates in demographic quantities such as average planet radii, the injected changes happen on the planetary level: We changed each planet's transit radius based on its individual set of properties and the associated predictions from steam atmosphere and water retention models. Relevant properties are a planet's mass M, its net instellation S, and its bulk water inventory expressed as the total planetary water mass fraction x_{H_2O}. We consider the following cases (see Figure 3):

Non-runaway planets retain the radius assigned based on exoplanet occurrence rates (see Sect. 2.3). This case serves as our null hypothesis.

We consider as *runaway* planets those planets that absorb a stellar flux higher than a dayside-averaged threshold instellation S_{thresh}. For all planets absorbing an instellation exceeding $S_{\mathrm{thresh}} = 280\,\mathrm{W\,m^{-2}}$, we assume an inflated transit radius due to a steam atmosphere. While the actual instellation threshold for a runaway climate depends on planetary albedo, surface gravity, and clouds (Pluriel et al. 2019; Turbet et al. 2021; Pierrehumbert 2022), this value was found to be a typical limit for the flux a planet can emit in a runaway greenhouse situation (Goldblatt et al. 2013; Kopparapu et al. 2013; Leconte et al. 2013a; Hamano et al. 2015; Salvador et al. 2017; Katyal et al. 2019; Boukrouche et al. 2021; Lichtenberg et al. 2021a). This choice translates to about 1.18 times the instellation of present-day Earth with a fixed albedo of 0.3, which compares favourably to previous climate simulations (Leconte et al. 2013a; Wolf & Toon 2015). We adopt the same threshold instellation for all host star spectral types.

To quantify the radius change, we applied the mass-radius relationships derived by Turbet et al. (2020) using a 1D inverse radiative-convective model (Turbet et al. 2019). Their calculations rely on the same mass-radius relations for rocky interiors that we apply for our non-runaway planets (Zeng et al. 2016). For each planet above the instellation threshold, we assigned the predicted radius for the given water mass fraction and planet mass.

Nominally, the above models assume a *dry melt* without dissolved volatiles. Here, however, we consider a *wet melt* magma ocean and take into account a radius decrease from retention of water in the melt (Dorn & Lichtenberg 2021). The impact of the water distribution between melt and atmosphere on the change of the

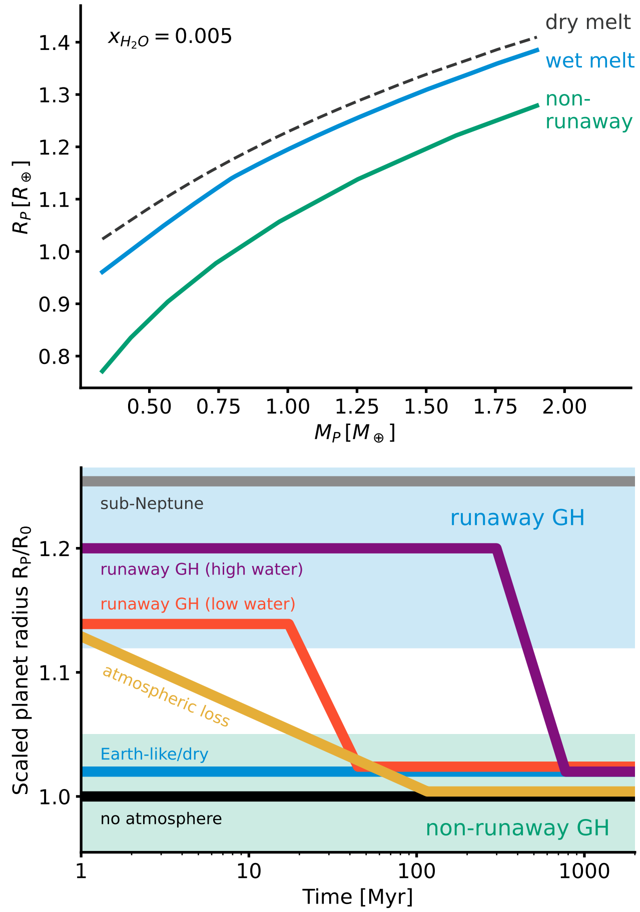

Figure 3. *Top*: Mass-radius relationships for a bulk water mass fraction $x_{H_2O} = 0.005$ and different planet states. Green: planets with a solid mantle and no steam atmosphere. Dashed: planets with steam atmospheres. Blue: planets with steam atmospheres and including the effect of water retention in the melt. Steam atmospheres cause a significant radius increase, which is slightly reduced when water retention in the melt is considered. *Bottom*: Radius evolution of different planet types, illustrating degeneracies and potential for confusion among planet classes. Shown is a schematic time evolution of the transit radius normalized to the atmosphere-free radius R_0 for different scenarios. Planets can move between planet classes through processes such as atmospheric loss and desiccation, which ultimately ends a runaway greenhouse phase on a timescale dependent on a planet's water content.

transit radius depends on the planet's mass and water content and is generally small compared to the radius inflation from the steam atmosphere. We computed radius deviations between a wet magma ocean and a solid mantle following Dorn & Lichtenberg (2021) and assuming a tropopause pressure $P_{\rm iso} = 0.1$ bar. We then added the (in almost all cases negative) radius deviations to the inflated planet radii computed for the dry melt case.

We illustrate the mass-radius relations of the three cases in Figure 3 where a fiducial bulk water mass fraction of $x_{H_2O} = 0.005$ is assumed. In the following, we only distinguish between the non-runaway greenhouse and wet melt scenarios.

To account for planets unable to sustain a steam atmosphere over extended time spans, as well as evolutionary effects such as desiccation through water photodissociation and H escape (see bottom panel of Figure 3), we introduce a dilution parameter $f_{\rm rgh}$. It represents the fraction of planets above the instellation threshold whose atmospheres are currently inflated due to a runaway greenhouse climate. Our simulation setup is such that all planets receiving a net instellation $S < S_{\rm thresh}$ follow the non-runaway greenhouse relation, and a fraction $f_{\rm rgh}$ of the planets with $S > S_{\rm thresh}$ follow the wet melt relation. The choice $f_{\rm rgh} < 1$ reflects the fact that planets – despite a high irradiation – can evade a runaway greenhouse climate. This situation may, for instance, arise in the absence of an atmosphere or of volatiles that could form a steam atmosphere. In the following, we test if and under what conditions this parametrization causes a demographic trend that is large enough to be detected with high significance.

4. EXOPLANET SURVEY SIMULATIONS AND HYPOTHESIS TESTING

The survey module of `Bioverse` converts the synthetic planet sample into a set of uncertainty-laden measurements on a subset of that sample. This task includes selection of the targets, application of detection biases, and conducting simulated measurements, all of which are specific to the particular survey. For each planet-level measurement such as transit radius or instellation, we draw the measured value from a normal distribution centered on the true value with a standard deviation set by the survey's precision. We then follow a Bayesian hypothesis testing approach to assess various realizations of simulated surveys in terms of their ability to detect and characterize the runaway greenhouse transition.

4.1. *Detection bias, target selection, and sensitivity*

Not all transiting planets are detectable with the same likelihood and detection biases have an impact on the demographic measurements we are interested in. A detailed characterization of the detection biases of individual missions would not be justifiable given the uncertainties of the theoretical predictions. Instead, we derived generic observing limits that reflect the limitations of state-of-the-art transit surveys.

A successful transit detection requires a sufficient signal-to-noise ratio, which is sensitive to the achieved photometric precision. *PLATO* (PLAnetary Transits and Oscillation of stars) is an ESA mission designed to characterize terrestrial planets in the habitable zones of Sun-like stars via long-term high-precision photometric monitoring of a sample of bright stars (Rauer et al. 2016). In line with this requirement, *PLATO* is designed to enable the detection of a 80 ppm transit signal (Matuszewski et al. 2023; ESA 2017). To reflect its sensitivity, we chose a minimum transit depth of 80 ppm as a detection limit and consider only measurements of planets exceeding this threshold. We further exclude target stars with *Gaia* magnitudes $M_{\mathrm{G}} > 16$.

The runaway greenhouse effect becomes obsolete both for very small instellations and where no atmosphere can be maintained due to proximity to the host star and resulting atmospheric erosion. Ensuring to stay well clear of such regions, we clear our sample from all planets with a net instellation $S < 10\,\mathrm{W\,m^{-2}}$ or $S > 2000\,\mathrm{W\,m^{-2}}$. We further consider only rocky planets with masses below $2\,\mathrm{M_\oplus}$.

4.2. *Measurements and their uncertainties*

Under real-world conditions, the planetary properties in question can only be probed with a finite precision that is specific to each exoplanet mission. *PLATO*'s definition study report (ESA 2017) states precision requirements for planet radii (3 %), planet masses through radial velocity (RV) follow-up (10 %), and stellar masses, radii, and ages (10 %). We adopted these estimates and assumed a 10 % error on instellation measurements.

Since planetary bulk density $\rho \propto R_{\mathrm{P}}^{-3}$, we expect a stronger runaway greenhouse signal when measured through bulk density instead of transit radius. We thus simulated measurements of planetary densities assuming the mass-radius relation defined above. For uncertainties in bulk density measurements, we propagated the errors of the mass measurements assuming $\sigma_{\mathrm{M_P}} = 10\,\%$.

4.3. *Hypothesis tests*

We now turn to quantifying the ability of the simulated surveys to detect the habitable zone inner edge discontinuity and to constrain parameters associated to the runaway greenhouse transition. To do this, we rely on a Bayesian hypothesis testing approach where we quantify the evidence of a hypothesis over another based on the (simulated) data. For our specific problem, this implies comparing evidences for a demographic imprint of the runaway greenhouse effect to its absence. As a null hypothesis, we consider the case where the planetary radius distribution is independent of the instellation,

$$H_0(\theta, S) = \theta, \tag{3}$$

where θ is the set of parameters defining the radius distribution. We further define an alternative hypothesis that describes radius changes due to runaway greenhouse climates and inflated steam atmospheres. As motivated above, this hypothesis takes the form of a step function in net instellation S, where the step occurs at the outer edge of the runaway greenhouse region. Our main observable shall be the average transit radius in the planet population on either side of this threshold. The runaway greenhouse hypothesis is then defined as

$$H_{\mathrm{rgh}}(\theta, S) = \begin{cases} H_0, & S \leq S_{\mathrm{thresh}} \\ \langle R_{\mathrm{P}} \rangle (f_{\mathrm{rgh}}, \Delta R_{\mathrm{stm}}, \Delta R_{\mathrm{wtr}}), & S > S_{\mathrm{thresh}}. \end{cases} \tag{4}$$

Here, f_{rgh} is the fraction of planets above the instellation threshold experiencing a runaway greenhouse effect. ΔR_{stm} and ΔR_{wtr} are predicted radius changes from the steam atmosphere and water retention models, respectively. They are assumed to act additively on the planet radii and thus on their average $\langle R_{\mathrm{P}} \rangle$.

The only free parameter of the null hypothesis, which assumes the average transit radius to be independent of instellation, is the predicted mean radius $\langle R_{\mathrm{P}} \rangle$. The functional form of the runaway greenhouse hypothesis is more complex: Besides the mean radius of planets outside the threshold $\langle R_{\mathrm{P}} \rangle_{\mathrm{out}}$, which is a nuisance parameter necessary to define the hypothesis, it relies on the threshold instellation for the "step" S_{thresh}, the planetary bulk water mass fraction x_{H_2O}, and the dilution factor f_{rgh}. For hypothesis tests based on bulk density instead of radius, we proceeded in the same way and substituted R_{P} by the bulk density ρ.

A sensible choice of priors is central for evidence estimation via nested sampling. As the parameters of interest are poorly constrained by previous data, we used relatively uninformative priors to sample the entire physically plausible parameter space. For S_{thresh}, we chose a uniform prior in $[10, 1000]\,\mathrm{W\,m^{-2}}$. We sampled x_{H_2O} from a log-uniform distribution to imply scale-invariant ignorance. Its boundaries $[10^{-5}, 0.1]$ are motivated by the water mass fractions covered by the geophysical models (Sect. 3). For f_{rgh}, we chose a uniform prior in $[0, 1]$. Finally, we adopted a broad, uniform prior for $\langle R_{\mathrm{P}} \rangle_{\mathrm{out}}$ bound by $[0.1, 15]\,\mathrm{R_\oplus}$. In the case of measuring bulk densities instead of transit radii, we drew uniformly from $[1, 6]\,\mathrm{g\,cm^{-3}}$.

The measured radii $R_{\mathrm{P,i}}$ or bulk densities ρ_{i} cannot be directly used for the hypothesis tests as they include intrinsic scatter that is not caused by measurement errors. H_{rgh} and H_0 should thus be tested against a statistical estimator that represents the population mean. To avoid binning and the artificial patterns it may introduce, we chose to test our hypotheses against a simple moving average SMA along the instellation axis with a window of size 25 centered around each measurement.[3] We further computed the uncertainty of this moving average by propagating the individual measurement errors and applying a rolling standard error of the mean.

As our procedure involves random sampling of the model parameters θ, we need to define the probability of obtaining a data set given the model parameters, i.e., a likelihood function $\mathcal{L}$. We assumed here that the individual moving averages SMA_i are measured with a normally distributed uncertainty σ_{SMA_i} and adopted a normal distribution

$$\mathcal{L}(SMA \mid \boldsymbol{\theta}) = \prod_i^N \frac{1}{\sqrt{2\pi\sigma_{SMA_i}^2}} \tag{5}$$

$$\times \exp\left(-\frac{(SMA_i - H(\boldsymbol{\theta}, S_i))^2}{2\sigma_{SMA_i}^2}\right). \tag{6}$$

Here, $H(\boldsymbol{\theta}, S_i)$ corresponds to the functional form of the runaway greenhouse or null hypothesis.

4.4. *Bayesian model comparison*

We can now assess the relative plausibility of H_{rgh} and H_0 given the synthetic data we have generated, assigning equal a priori probabilities to these models. This is done by comparing the Bayesian evidence $\mathcal{Z}$ of the models, which we estimated with the nested sampling (Skilling 2004) algorithm *dynesty* (Speagle 2020). We initialized the sampler with the priors defined above to let it estimate the evidence and sample the posterior distributions. Our criterion to reject the null hypothesis is

$$\Delta \ln \mathcal{Z} = \ln \mathcal{Z}_{\mathrm{rgh}} - \ln \mathcal{Z}_0 > 3. \tag{7}$$

5. RESULTS

5.1. *Statistical signature of the runaway greenhouse threshold*

To characterize the population-level imprint of individual radius changes, we generated a generic planet population with an injected runaway greenhouse effect assuming a water fraction $x_{\mathrm{H_2O}} = 0.005$. Figure 4 shows the resulting planetary radii. When ordered in orbital period space, the different planet types overlap, diluting the demographic imprint. With net instellation as an independent variable, planets above and below the runaway greenhouse threshold separate: The runaway greenhouse-induced radius inflation introduces a discontinuity of average planet radii and bulk densities as a function of stellar irradiation. We also show the predictions of observable average planet radii from the statistical hypotheses defined above. Within the runaway greenhouse regime, an average radius change of 15 % occurs. This pattern is consistent with the injected radius inflation as predicted from the atmospheric models (see Appendix A.2 for an investigation of the interplay between model predictions and our synthetic planet population).

5.2. *Testability of the runaway greenhouse hypothesis*

Figure 5 shows a prototypical statistical detection of the habitable zone inner edge discontinuity. Before we study limiting cases of such a detection below, we first demonstrate the interpretation process based on an optimistic scenario where the sample of characterized planets is large ($N = 500$) and the measurement uncertainties are small ($\sigma_R = 2\,\%, \sigma_S = 5\,\%$). Here, we assumed that the fraction of those planets irradiated stronger than S_{thresh} that have runaway greenhouse climates is $f_{\mathrm{rgh}} = 0.8$, and we chose a water mass fraction of $x_{H_2O} = 0.005$ for each planet. In this case, the habitable zone inner edge discontinuity was detected with high significance ($\Delta \ln \mathcal{Z} \approx 100$).

With such a strong signal, we can attempt an inference of the parameters defining the injected effect. Figure 6 shows the posterior distributions of S_{thresh}, x_{H_2O}, and f_{rgh} as determined by the nested sampler. The threshold instellation can be accurately constrained. Both a higher water mass fraction and a higher dilution factor lead to larger average radii, thus these parameters are strongly correlated.

Figure 7 explores the statistical power of the hypothesis test achieved in the above scenario for different combinations of the poorly constrained parameters x_{H_2O} and f_{rgh}. It is highest for large water inventories and large dilution factors. For all but very low water fractions, f_{rgh} dominates this trend: It enters linearly into the average planet radius, whereas the contribution of x_{H_2O} - as predicted by the geophysical models - is sublinear with a power-law exponent of ~ 0.3. Within the framework of our model and as long as f_{rgh} is larger than ~ 0.2, a sample size of 500 is sufficient for a 50 % detection rate even for water ratios as low as 10^{-3}.

5.3. *Detecting the runaway greenhouse transition with PLATO*

To simulate the transit survey of ESA's *PLATO* mission, we considered a volume-limited sample with a size according to projections and including all stellar spectral types. Given *PLATO*'s expected radius precision, we find that a yield of ~300 is needed for a significant

[3] See Appendix A.1 for a robustness test using a different estimator.

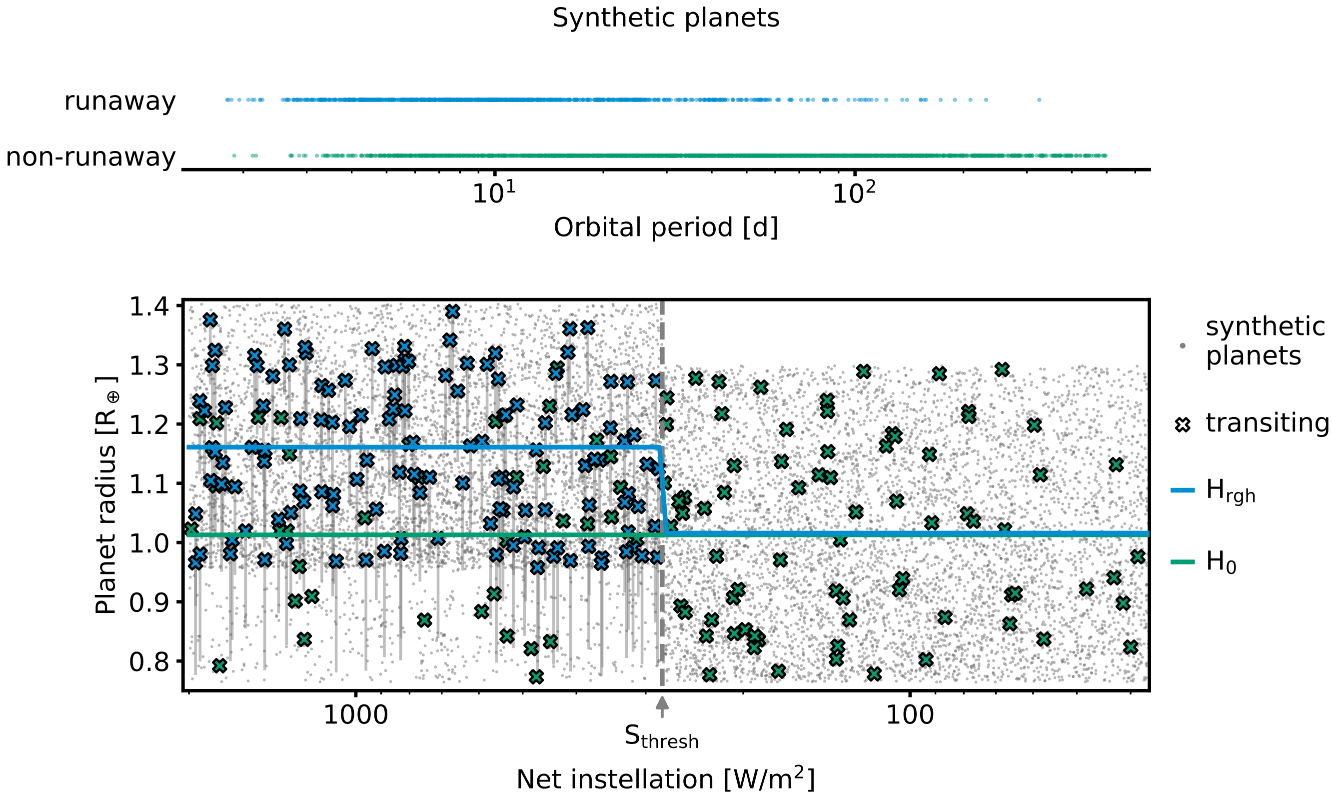

Figure 4. Synthetic planets above and below the runaway greenhouse threshold. *Top*: Planet state as a function of orbital period. Planets with and without a runaway greenhouse climate mix and are not distinguishable in orbital period space. *Bottom*: Transit radii of synthetic planets with injected radius deviation as a function of net instellation. Only the planets marked as transiting are observable. Above the runaway greenhouse threshold $S_{\mathrm{thresh}} = 280\,\mathrm{W\,m^{-2}}$, some planets maintain their original radii (green crosses) whereas some have their transit radius inflated (blue crosses) by the amount indicated with gray lines. The sharp boundary at S_{thresh} causes a discontinuity in the average planet radius (blue line). This runaway greenhouse hypothesis can be tested against the null hypothesis H_0 (green line), where average radii are independent of instellation.

detection if the fraction of runaway greenhouse planets $f_{\mathrm{rgh}} = 0.1$ (see Figure 8). The minimum needed fraction rises to 0.2 for $N = 100$. For much smaller samples, only an optimistically strong signal is likely to be detected.

5.4. *Statistical power of different mission designs*

5.4.1. *Additional planet mass measurements*

Comparing a measurement of the habitable zone inner edge discontinuity in radius space with a measurement in density space (which requires planetary mass measurements), a stronger detection occurs in the latter case: With an optimistic choice of geophysical parameters (see Sect. 5.2), the average measured radius change is 15 % whereas the average density change is −33 %.

Figure 8 shows that investigations of the discontinuity are more constraining when radius measurements can be augmented with mass measurements: At unchanged sample size, the difference in Bayesian evidence can be up to an order of magnitude larger. Consequently, we achieve a statistically significant detection with smaller samples or lower dilution factors f_{rgh}. A density-based survey of 100 targets is roughly equivalent to a radius-based survey of 300 targets. At $N = 100$, pure radius measurements require $f_{\mathrm{rgh}} \gtrsim 0.2$ whereas bulk density measurements enable a detection from $f_{\mathrm{rgh}} \gtrsim 0.1$.

5.4.2. *Dependence on host star spectral type*

Since the incident radiation at a given orbital distance depends on the spectral type of the host star, the relative number of planets on either side of S_{thresh} is different for FGK and M dwarfs. We tested the detectability of the habitable zone inner edge discontinuity when only FGK or only M dwarfs are considered (see Figure 8). All other parameters of the climate models are kept the same. The samples are volume and magnitude-limited to reflect the target counts of *PLATO*'s provisional Long-duration Observation Phase fields (15996 FGK stars in the P1 and P2 samples, 33948 M stars in the P4 sample, Nascimbeni et al. 2022). The resulting M dwarf planet sample is significantly larger with 228 ± 14 planets compared to 40 ± 6 planets in the FGK sample. No significant detection is possible in the pure FGK sample,

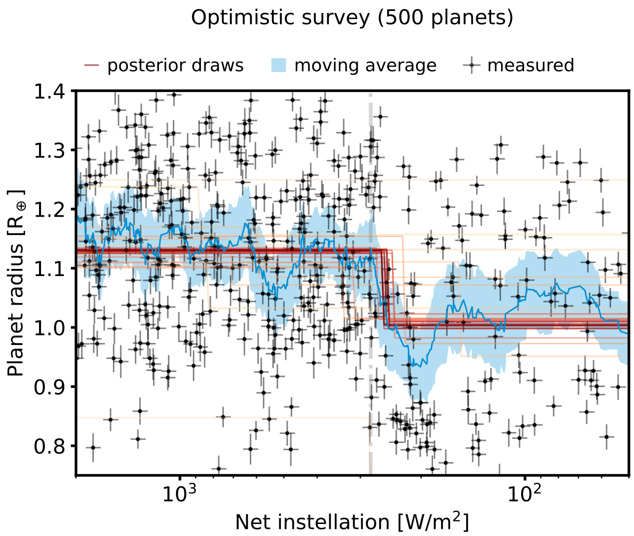

Figure 5. Detection of the runaway greenhouse threshold. From simulated radius and instellation measurements of a large ($N = 500$) survey, we compute the moving average (blue confidence intervals) and fit the runaway greenhouse hypothesis to it (Eqn. 4, random draws from the posterior in red). The pattern is detected with high significance.

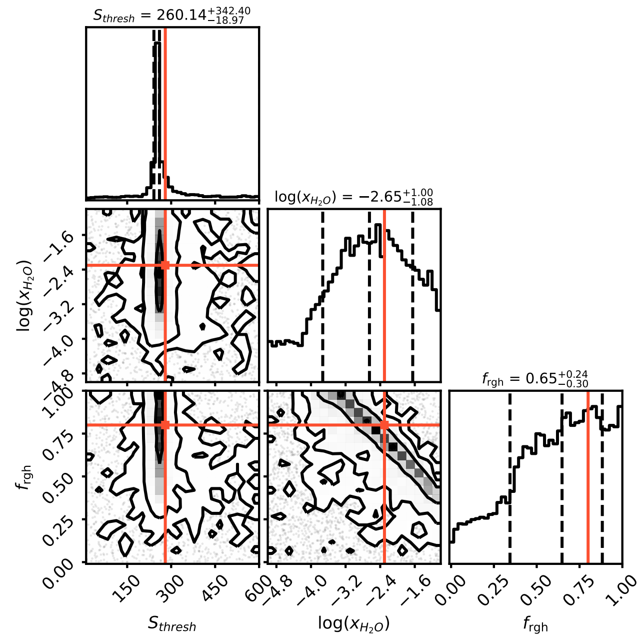

Figure 6. Retrieved posterior distribution of key parameters in the optimistic scenario. The density maps in each panel show relationships between and marginalized distributions of the threshold instellation $S_{\rm thresh}$, the bulk water mass fraction x_{H_2O}, and the dilution factor $f_{\rm rgh}$ as they could be retrieved with a high-precision transit survey and a sample of 500 planets. True values of the parameters for the injected effect are shown in orange. The threshold instellation can be reasonably constrained; the predominant water fraction and the fraction of planets with runaway greenhouse climates are degenerate.

independent of the assumed geophysical parameters. In the M dwarf sample, the evidence threshold is reached around $f_{\rm rgh} \sim 0.2$, similar to the case above where all spectral types are considered.

5.4.3. *Constraining the threshold instellation*

Although the exact location of the runaway greenhouse transition depends on the stellar energy actually absorbed by the planet, a measurement of $S_{\rm thresh}$ would be a key constraint resulting from a detection of the habitable zone inner edge discontinuity. Here, we assess the ability of different mission concepts explored above to constrain this parameter. Figure 9 shows posterior distributions from a grid of inferences together with the true values of the injected signal for different fractions $f_{\rm rgh}$. We consider three cases: only radius measurements, radius and mass measurements, and radius and mass measurements of only planets orbiting M dwarfs. The simulations otherwise represent the simulated *PLATO* example described above. We chose a planetary sample size of $N = 100 \pm 10$, as this was found to be a threshold case in Sect. 5.3.

We find that retrievals from radius measurements alone require high fractions of greenhouse climate-bearing planets to achieve an accurate constraint on $S_{\rm thresh}$: dilution factors $f_{\rm rgh} \gtrsim 0.5$ yield posterior probability distributions that are condensed at the order of magnitude of the true value; accurate constraints to within ± 0.25 dex of the truth are reached only from $f_{\rm rgh} \approx 0.8$.

In contrast, if planet masses are available and the hypothesis test is conducted in bulk density space, useful constraints emerge already from about $f_{\rm rgh} \approx 0.35$. Accuracy and precision of the retrievals are improved.

A sample containing only planets around M dwarf yields still better performance and result in the overall best accuracy and precision. The reason is that these planets contribute most to the statistical power of the retrieval.

6. DISCUSSION

6.1. *Statistical imprint of exoplanet climates*

We showed in Sect. 5.1 that injecting the theoretically predicted radius inflation effect into a synthetic planet population following the currently known demographics leaves a distinct pattern in the radius and density distribution as a function of instellation. The transit radius inflation was suggested before as an observational diagnostic to probe the runaway greenhouse tran-

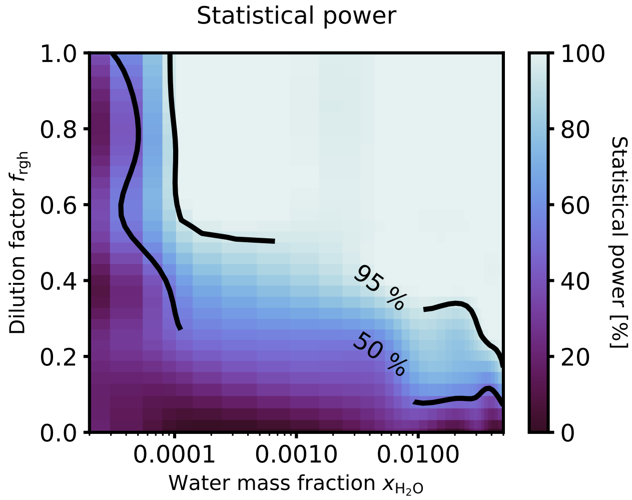

Figure 7. Statistical power of the runaway greenhouse hypothesis test as a function of model parameters. For a sample size $N = 500$, the color code shows the fraction of simulations resulting in a sound detection ($\Delta \ln \mathcal{Z} > 3$) for different combinations of bulk water mass fraction and dilution factor. Higher values in either parameter result in a more reliable detection. For water mass fractions $\gtrsim 10^{-4}$, the statistical power largely depends on the fraction of greenhouse climate planets in the sample.

sition (Turbet et al. 2019), and our simulations show quantitatively how the contributions of the individual radius changes combine to create a significant demographic signal. Its strength depends on largely unknown factors such as the planetary volatile content, but turned out to be well in the detectable range under reasonable assumptions of these factors.

Our finding that the expected habitable zone inner edge discontinuity is strong except for extremely low water mass fractions gives reason for optimism regarding its detection. It also presents a potential for constraints on the water inventory of terrestrial planets in the case of a non-detection. Such constraints will provide insight into whether the initial water content of rocky planets is varied by systematic inter-system effects (e.g., Raymond et al. 2004; Mulders et al. 2015; Sato et al. 2016; Lichtenberg et al. 2019; Lichtenberg & Krijt 2021; Lichtenberg & Clement 2022) or if there is a predominant pattern of volatile-enrichment across planetary systems that is only modified by intra-system effects such as planet migration (Schlecker et al. 2021a) or atmospheric escape (Owen & Wu 2016). Ultimately, such measurements will shed light on how delivery and loss effects during rocky planet formation and evolution shape the diversity of exoplanetary climates. Overall, probing the runaway greenhouse discontinuity appears to be the most promising approach toward a first empirical test of the habitable zone concept.

6.2. *Detectability of the habitable zone inner edge discontinuity*

We showed in Sect. 5.2 that under favorable conditions, a sufficiently large (500 planets) photometric survey is likely to detect the demographic imprint of the runaway greenhouse transition and accurately constrain the associated threshold instellation. Of course, even assuming capable instrumentation and an optimal survey design, our current models may not capture fully the complexity of trends in the geophysics and demographics of small planets. The detectability of the runaway greenhouse threshold is thus a function of both survey design and the diverse outcomes of rocky planet formation and evolution. In the following, we will explore the key factors that may influence the emerging demographic signal.

6.2.1. *Key factors influencing tests of the runaway greenhouse hypothesis*

What influences the probability of correctly rejecting a false null hypothesis? We revidentified six drivers of the diagnostic power for detecting the runaway greenhouse transition with a transit survey. Many of these factors directly influence the fraction of planets currently in runaway greenhouse states, which in our model is represented by the dilution factor f_{rgh}.

- Occurrence rate of planets forming steam atmospheres
- Planetary evolution and duration of the steam atmosphere phase
- Prevalent water inventory
- Size and composition of the planetary sample
- Radius measurement precision
- Availability and precision of mass measurements

We will now briefly explore the above drivers.

Occurrence rate of planets forming steam atmospheres: The runaway greenhouse climate relies on sufficient amounts of atmospheric water vapor that can act as a greenhouse gas. It was shown that already about ∼10–20 bar of water vapor − corresponding to a minor fraction of one Earth ocean and thus the lower limit of water on Earth − is enough to sustain sufficiently high surface temperatures to keep the planet in a magma ocean stage (Boukrouche et al. 2021; Lichtenberg et al. 2021). However, recent simulations accounting for radiative–convective profiles of near-surface

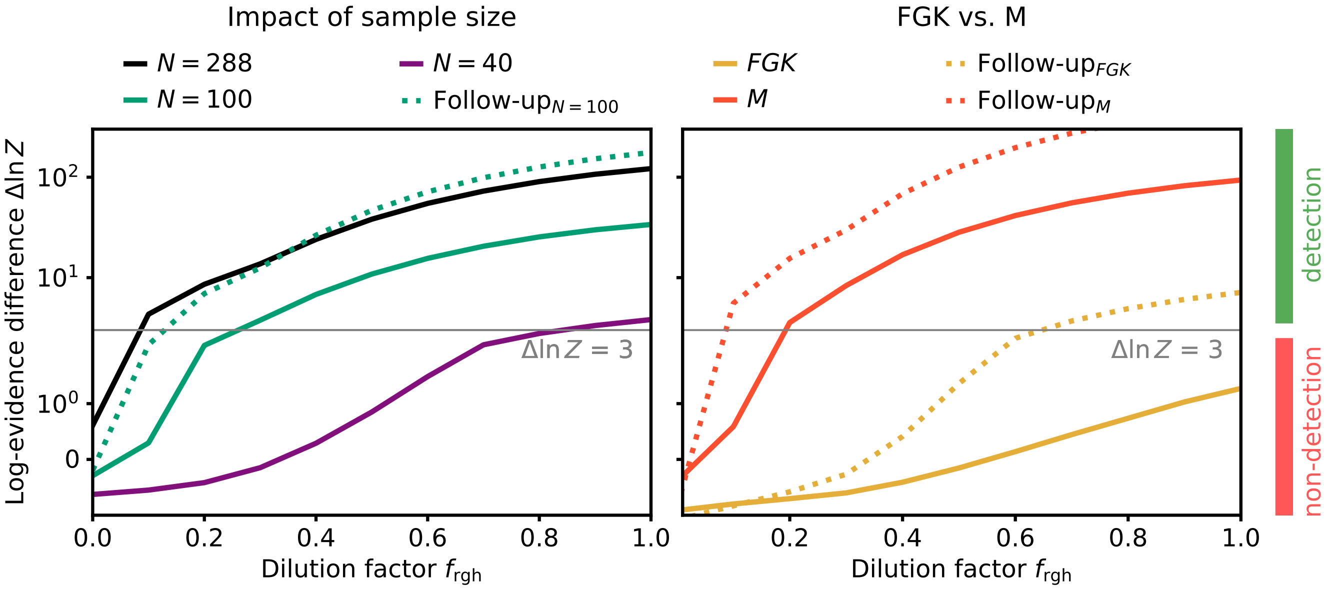

Figure 8. Expected delta-evidences as a function of the fraction of planets with runaway greenhouse climates for different versions of the *PLATO* survey. The median values of randomized survey simulations are shown; $\Delta \ln Z > 3$ (gray horizontal line) is considered sufficient evidence to reject the null hypothesis. *Left:* For a large planet yield of $N \approx 300$, even small dilution factors ~ 0.1 allow a detection. A sample of 100 planets is sufficient if their masses are constrained to within 10 % (dotted green line). Without such follow-up measurements, sufficient diagnostic power can only be achieved with this sample if $f_{\rm rgh} \gtrsim 0.2$. Even smaller samples are unlikely to yield a significant detection. *Right:* Evidences when only FGK or only M dwarfs are considered. Only M dwarfs host enough planets on both sides of the threshold instellation to allow a reliable detection of the habitable zone inner edge discontinuity.

atmospheric layers suggest the existence of cooler pure-steam runaway greenhouse states that do not necessarily yield a molten surface (Selsis et al. 2023). Climate state and atmospheric structure, as well as the fraction of planets fulfilling the requirements of a steam atmosphere have an impact on the amplitude of the demographic imprint of the runaway greenhouse transition. From a planet formation perspective, the incorporation of water into planets in the terrestrial planet zone is a standard expected outcome (e.g., Zeng et al. 2019; Venturini et al. 2020; Emsenhuber et al. 2021; Schlecker et al. 2021a; Burn et al. 2021). But while commonly considered volatile delivery channels suggest a fraction of planets to be volatile-poor, the incorporation of hydrogen into even the driest planetary materials known in the solar system (McCubbin & Barnes 2019; Piani et al. 2020; Jin et al. 2021) suggests that hydrogen is present in all rocky planets upon formation. Accreted hydrogen in nominally dry planetary materials react with mantle oxygen to form substantial amounts of water inside of the planet during the magma ocean phase (Ikoma et al. 2018; Kite & Schaefer 2021; Kimura & Ikoma 2020, 2022). Enhanced equilibration between the core, mantle, and atmosphere during magma ocean evolution of rocky exoplanets further enhances this process (Lichtenberg 2021; Schlichting & Young 2022). Therefore, even nominally dry planets generate substantial amounts of water during formation and early evolution. Reduced heating from short-lived radionuclides in extrasolar planetary systems increases the expected water abundance in exoplanet systems further, in particular for M dwarf systems (Lichtenberg & Clement 2022).

Planetary evolution and duration of the steam atmosphere phase: An inflated steam atmosphere can only be sustained until the planet has lost its water. Depending on host star spectral type, planetary mass, and composition, planets can spend from a few Myr to several Gyr in runaway greenhouse climates (Hamano et al. 2015; Luger & Barnes 2015), and only planets observed during this phase will contribute to the habitable zone inner edge discontinuity. However, the delivery uncertainty is much greater than the predicted loss rates of water by atmospheric escape, which typically is limited to in total a few tens of terrestrial oceans per Gyr (Wordsworth et al. 2018) on even the most irradiated exoplanets (see discussion in Lichtenberg & Clement 2022). The finite duration of steam atmosphere phases is a main factor for diluting the habitable zone inner edge discontinuity, and it leads to an increased likelihood of detecting this imprint for younger planetary systems. Preferen-

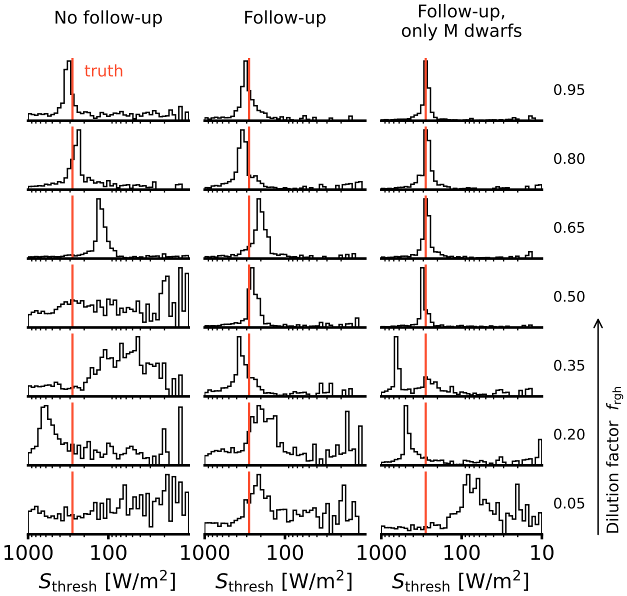

Figure 9. Retrieved posterior distributions of the threshold instellation for different survey realizations. All cases assume $x_{H_2O} = 0.005$ and a planet sample size $N = 100 \pm 10$; The fraction of planets with runaway greenhouse climates varies across rows. Orange lines show the true value of the injected signal. Accuracy and precision of the constraint on S_{thresh} generally improve with higher f_{rgh}. Bulk density-based inferences improve the constraints, and M dwarf samples yield the highest accuracy and precision.

tial selection of younger systems could therefore be of advantage in a targeted survey.

Prevalent water inventory: The magnitude of radius change at the runaway greenhouse threshold is sensitive to the water mass fraction. As a result, the statistical abundance of water in terrestrial planets impacts the strength of the demographic pattern: The higher the water content and the higher the fraction of planets in runaway greenhouse climates, the greater the likelihood that a discontinuity is detectable. However, dissolution into the magma ocean and atmospheric inflation show non-linear coupling: the more water there is in the atmosphere, the more will be dissolved (Dorn & Lichtenberg 2021), leading to a convergence in radii until saturation. Most important for the present work, however, is the qualitative dichotomy between sub-runaway and runaway planets, which outcompetes radius variations within each of these climate states due to a changing water mass fraction (Turbet et al. 2020). If a planet hosts a significant water inventory that is not easily stripped by atmospheric escape (Johnstone 2020), then the statistical power of our model is high (see Figure 7).

Size and composition of the planetary sample: The significance of a statistical trend increases with a larger sample size. In addition, the sample must include planets on both sides of the instellation threshold. This is only likely for low-mass host stars due to the strongly distance-dependent detection bias associated with the transit method and the temporal coverage of upcoming transit missions.

Radius measurement precision: The more precise individual planet radii can be determined, the more pronounced the discontinuity will be. Good *accuracy* is less important, as long as it does not have a systematic error scaling with stellar irradiance.

Availability and precision of mass measurements: For simple geometric reasons ($\rho \propto R^{-3}$), the expected discontinuity at the habitable zone inner edge is stronger when measured in bulk density than it is in planet radius space. If transiting planets can be followed up to obtain mass measurements, the statistical significance increases.

Besides these main factors, uncertainties in the measured instellations can influence the result, although they are typically small due to the very precise orbital period measurements available for transiting planets. This can be different for young host stars when their ages cannot be well constrained; in particular, the long pre-main sequence phase of M dwarfs shows a large variation in bolometric luminosity (see Figure 2).

6.2.2. *False positive scenarios*

Runaway greenhouse climates are not the only physical mechanism that may cause a change in transit radius for a subset of planets. Alternatives include atmospheric loss due to either photoevaporation through high-energy radiation by the host star (e.g., Ikoma & Hori 2012; Owen & Wu 2013; Jin et al. 2014; Mordasini 2020) or due to residual heat from the planet's interior shortly after formation (Ginzburg et al. 2016, 2018; Gupta & Schlichting 2019). Both processes are being discussed as potentially sculpting the observed bimodality in the radius distribution of small exoplanets (Fulton et al. 2017; Van Eylen et al. 2018), and both lead to a decrease of planet radius for planets close to their host star (Pascucci et al. 2019; Bergsten et al. 2022). This is distinct from the radius inflation introduced by runaway greenhouse climates. For example, the innermost planet in the K2-3 system has an increased radius compared to its outer siblings, contrary to what would be expected from atmospheric escape (Diamond-Lowe et al. 2022).

Other false positive contributions may stem from potential unknown occurrence rate gradients in radius-instellation space, especially if these variations are similar to the expected habitable zone inner edge discontinuity. Although an abrupt pattern at the expected location of the transition seems unlikely, examples of steep occurrence rate density changes exist. An example is the "Neptune desert", a triangular region in period-radius space of low planet occurrence (Szabó & Kiss 2011; Mazeh et al. 2016; Dreizler et al. 2020). The shape of this region is such that smaller planets become less frequent the closer to the star they are, which to some degree resembles the pattern introduced by the instellation dependency of the runaway greenhouse transition. However, the Neptune desert occurs at smaller orbital periods and is sensitive to the planet radius (Szabó & Kiss 2011), which is not expected for the runaway greenhouse transition.

Luque & Pallé (2022) found that small planets orbiting red dwarfs can be classified into three density regimes with a particularly strong separation between planets consistent with a pure rocky and those consistent with a water-rich composition. This trend does not represent a false positive scenario for the habitable zone inner edge discontinuity, since no strong dependency on instellation has been found or is expected. A population of "water worlds" with low bulk densities on a wide range of orbits would merely attenuate the statistical runaway greenhouse imprint. If the dichotomy forms primordially through migrated planets that accreted from different regions of their protoplanetary disk (Venturini et al. 2020; Burn et al. 2021; Schlecker et al. 2021a,b) or from inter-system variations in the desiccation of volatile-rich planetesimals (Lichtenberg et al. 2019; Lichtenberg et al. 2021b; Lichtenberg & Krijt 2021; Lichtenberg & Clement 2022; Bonsor et al. 2023), systems of all ages can be affected by this attenuation.

6.2.3. *Atmospheric spectral signatures*

We currently see four potential lines of discriminating atmospheric signatures associated with runaway climates in the exoplanet population. (i) Detecting the atmospheric windows of water vapor in the near- to mid-infrared. In a runaway greenhouse atmosphere, absorption is dominated by the opacity of water vapor, which has two prominent spectral features: one at 3.5–4.5 μm, and one between 8–20 μm (e.g., Boukrouche et al. 2021). Probing these features requires an instrument covering these wavelength ranges, for instance ELT METIS (Brandl et al. 2021), JWST MIRI (Rieke et al. 2015), or future missions such as *LIFE* (Bonati et al. 2019; Quanz et al. 2022; Dannert et al. 2022). Potentially the two-band filter capabilities of *PLATO* may offer insight into particularly pronounced spectral features in this runaway greenhouse regime (Grenfell et al. 2020). However, detecting water features in steam atmospheres may be obscured by high-altitude clouds that could potentially mute a transit signal as measured from peak to trough of an observed spectral line (Suissa et al. 2020; Fauchez et al. 2019). A better understanding of the role of clouds in this problem may be critical for observational constraints on the runaway climate of individual exoplanets. (ii) Post-runaway planets may be detectable through O_3 absorption due to build-up of abiotic oxygen, leftover from photochemical dissociation of water, and hydrogen loss (Wordsworth & Pierrehumbert 2014; Luger & Barnes 2015). (iii) Water loss in runaway greenhouse episodes would increase the atmosphere's D/H isotopic ratio, akin to the enhancement in Venus' present-day atmosphere (Kane et al. 2019, 2021). This may be detectable in high-resolution observations focusing on isotope-sensitive transitions (Lincowski et al. 2019; Mollière & Snellen 2019). (iv) Disequilibrium chemistry in tidally-locked runaway planets. It has been suggested that the atmospheric depth and the presence or absence of oceans on "sub-Neptunes" could be probed via the abundance of species that are photochemically destroyed in the upper atmosphere, and replenished from either thermochemical layers (Yu et al. 2021; Tsai et al. 2021) or at an ocean-atmosphere interface (Loftus et al. 2019; Hu et al. 2021). Atmospheric nitrogen and carbon compounds can be partitioned into magma (Grewal et al. 2022; Bower et al. 2022). Therefore, it may be possible to discern the presence of an underlying magma ocean if the presence of an atmosphere on a rocky exoplanet can be confirmed. This has been suggested to be done via (v) eclipse photometry (Mansfield et al. 2019; Koll et al. 2019) through the presence of a high albedo, which is expected to differ from the crystallized rock of a solidified magma ocean (Essack et al. 2020; Fortin et al. 2022). Spectral information from atmospheres of highly irradiated planets may also help to distinguish classical runaway greenhouse states from other climate regimes, such as a moist bistability (Leconte et al. 2013b).

6.2.4. *Detection in multi-planet systems*

As suggested by Turbet et al. (2019), an alternative approach for detecting the runaway greenhouse-induced radius inflation is to search for its "local" imprints in multi-planet systems. Systems harboring planets on both sides of the transition, such as TRAPPIST-1 (Gillon et al. 2016, 2017; Luger et al. 2017; Agol et al. 2021), K2-3 (Diamond-Lowe et al. 2022), or Kepler-138 (Piaulet et al. 2022), may show the predicted abrupt radius and density change, provided the initial volatile content was sufficient and complete desiccation has not yet occurred. While degeneracies remain in interpreting bulk density fluctuations within individual systems (e.g., Turbet et al. 2020; Dorn & Lichtenberg 2021), the detection of a consistent pattern in several such systems could be a convincing statistical evidence of the runaway greenhouse transition. The current sample of suitable systems is sparse: The California-Kepler Survey catalog (Fulton & Petigura 2018) contains only six planets with instellations $< 2\,S_\oplus$ and smaller than $2\,\mathrm{R}_\oplus$ in five multi-planet systems. Future additions to the multi-planet sample through missions such as *PLATO* are needed.

6.3. *Diagnostic power of near-future exoplanet missions*

Confirming or disproving the predicted habitable zone inner edge discontinuity will depend on the significance with which the null hypothesis can be excluded, which is a function of instrumentation and survey strategy. As discussed in Section 6.2.1, key drivers from a mission design perspective are sample size, photometric precision, and the availability of planets around low-mass host stars. We found that along these axes, *PLATO* will be the most favorable among the upcoming transit missions. The *PLATO* team has released an estimate on the number of exoplanets that will be characterized in the course of the main survey mission. With an expected transit radius precision of 3 % (ESA 2017) for hundreds of planets (Rauer 2021), the *PLATO* mission is comparable to the optimistic survey (see Section 5.2) in terms of sample size and precision. If successful, it should readily detect the predicted statistical imprint or, in case of a non-detection, provide strong upper limits on the occurrence rate of runaway greenhouse planets. The latter depends on the lifetimes of runaway greenhouse phases, which are a function of the initial water inventory of the planets (Hamano et al. 2015). Overall, it seems feasible to derive the typical water content of low-mass exoplanets from these occurrence estimates.

What other planned missions are suited to probe the habitable zone inner edge discontinuity? *Kepler* and *K2* have contributed a large number of discovered terrestrial-sized planets, but few of them are in the habitable zone and their host stars are typically too faint for RV follow-up with current instrumentation (Dressing & Charbonneau 2015).

Similarly, the Transiting Exoplanet Survey Satellite (*TESS*, Ricker et al. 2014) planet sample lacks temperate, small planets around bright host stars (Ment & Charbonneau 2023), as was expected from planet yield calculations (Barclay et al. 2018). As of March 22, 2023, the NASA Exoplanet Archive[4] lists 40 *TESS* candidate or confirmed planets smaller than $4\,\mathrm{R}_\oplus$ with lower estimated instellation than Earth's.

The ongoing *CHEOPS* mission was designed as a follow-up mission to search for transits of planets discovered with other techniques, in particular with radial velocity measurements (Benz et al. 2021). As such, it will provide precise radius constraints on a sample of small planets; however, only a small number of planets with orbital periods >50 d are being observed. This largely limits *CHEOPS*' coverage to planets within the runaway greenhouse regime, preventing a detection of the transition.

As *CHEOPS*, the Atmospheric Remote sensing Infrared Exoplanet Large survey (*Ariel*, Puig et al. 2016) will be a follow-up mission that is not designed to provide a large number of new radius measurements. *Ariel*'s primary targets are larger planets in the range of sub-Neptune to Jupiter-like planets. We thus do not expect a significant contribution to statistically exploring the inner edge of the habitable zone for Earth-sized planets.

While not primarily designed to detect transiting planets, the Galactic Bulge Time Domain Survey of the *Nancy Grace Roman Space Telescope* (Spergel et al. 2015) is expected to yield $\sim 10^5$ transiting planets on short orbits and constrain their radii in the course of its mission (Montet et al. 2017). $\mathcal{O}(1000)$ planets smaller than Neptune could be found around early to mid-M dwarfs, however, only a small fraction of them will reach into the habitable zone (Tamburo et al. 2023). We thus conclude that the *Nancy Grace Roman Space Telescope* could provide a useful sample to explore the runaway greenhouse transition, albeit with a predominant focus on water-rich (sub-)Neptunes (e.g., Pierrehumbert 2022).

Looking further ahead, the *Nautilus* Space Observatory concept (Apai et al. 2019a) represents a statistical mission able to provide precise radius measurements of a large sample (~ 1000) of small exoplanets. It employs a constellation of ~ 35 large-diameter ($D \sim 8.5\,\mathrm{m}$) telescopes using ultralight diffractive-refractive optical elements (Milster et al. 2020) with the primary goal to study the atmospheres of transiting exoplanets. Operating in an array mode, *Nautilus* would achieve the equivalent light-collecting area of a 50 m telescope. Its expected 1 ppm photometric precision (Apai et al. 2022) would enable precise radius measurements of a large sample, also through a low number of required visits per object. If realized, *Nautilus* will be a valuable instru-

[4] https://exoplanetarchive.ipac.caltech.edu

ment for characterizing the runaway greenhouse transition.

Other missions have been proposed that focus on characterizing exoplanet habitability, most notably the *Habitable Worlds Observatory* concept, which will build on the two precursor direct imaging concepts LUVOIR (The LUVOIR Team 2019) and HabEx (Gaudi et al. 2020). Similar science objectives are pursued by the Large Interferometer For Exoplanets (*LIFE*, Quanz et al. 2022) initiative, a mission concept utilizing a space-based mid-infrared nulling interferometer. Direct imaging surveys do not directly measure planetary radii and are primarily useful for providing context through atmospheric measurements of individual planets. However, because mid-infrared retrievals feature reduced degeneracy between cloud albedo and changes in surface area, the planet radius can be constrained in mid-infrared wavelengths (Defrère et al. 2018; Quanz et al. 2021). Mid-infrared direct imaging techniques, in particular, enable to study much deeper atmospheric layers than possible in reflected light (Wordsworth & Kreidberg 2022). Hence, the atmospheric structure can be retrieved for a wider variety of thermal and atmospheric scenarios (Alei et al. 2022; Konrad et al. 2022). Since the peak thermal emission in runaway greenhouse atmospheres will substantially decrease the star-to-planet flux ratio, mid-infrared wavelengths offer the possibility to probe the diversity of runaway climates in systems across different ages (Lupu et al. 2014; Bonati et al. 2019). Finally, mid-infrared surveys such as *LIFE* show a preference for M star planets (Quanz et al. 2022), which is beneficial for detecting the predicted habitable zone inner edge discontinuity (see Sect. 5.4.2). With a sample size of a few tens of planets crossing the runaway greenhouse transition, direct imaging missions will thus enable key insights into the compositional inventory of atmospheric volatiles and climate states (Hinkley et al. 2021; Currie et al. 2022), adding important details to a potential runaway greenhouse detection purely via transit radii.

As for exoplanets missions in their implementation phase, however, *PLATO* overall remains to be the most promising mission for an empirical confirmation or falsification of the runaway greenhouse transition at this time.

6.4. *Mission design trade studies*

To explore the impact of mission trades on the detectability of the habitable zone inner edge discontinuity, we simulated different survey designs and strategies and measured their capability to recover the trend and constrain its parameters. We assessed this capability based on two determinants: the likelihood that the mission is able to detect the injected trend, and the precision with which it can constrain the parameters of that trend.

6.4.1. *The value of follow-up campaigns*

The constraining power changes when additional information beyond planet radii is available for the characterized planet population. As runaway greenhouse phases leave a stronger imprint on bulk density than on planet radius (see Sect. 5.4.1), it would be beneficial to obtain constraints on planetary masses and test the runaway greenhouse hypothesis in density space instead of radius space. This way, useful results can be obtained under more pessimistic conditions, e.g., a low predominant water content of planetary surfaces and atmospheres or a smaller available planet sample. For a mission design similar to *PLATO* a density-based hypothesis test on about a third of the overall sample is equivalent to a pure radius-based analysis. At a fixed sample size, key parameters of the runaway greenhouse models can be more narrowly constrained when additional mass measurements are available.

Precise ground-based radial velocity measurements will be needed to provide these data, and a number of instruments are already successfully employed in characterizing terrestrial-sized exoplanets (e.g., Queloz et al. 2001; Pepe et al. 2010; Johnson et al. 2010; Ribas et al. 2023) and confronting these results with planet formation theory (e.g., Miguel et al. 2020; Burn et al. 2021; Zawadzki et al. 2021; Schlecker et al. 2022). A new generation of instruments on extremely large telescopes such as *G-CLEF* on the *Giant Magellan Telescope* (Szentgyorgyi et al. 2016), *ANDES* on the *European Extremely Large Telescope* (Marcantonio et al. 2022), or *MODHIS* on the *Thirty Meter Telescope* (Mawet et al. 2019) will open up the discovery space even further.

Recently, NASA and the National Science Foundation (NSF) commissioned an "Extreme Precision Radial Velocity Initiative" (Crass et al. 2021) to develop methods and facilities for precise mass measurements of temperate terrestrial planets. Their findings highlight that such measurements are costly, and therefore follow-up efforts may only be available for a subsample of the targets of a mission of *PLATO*'s scale. The diagnostic power of the hypothesis tests we demonstrated here may be improved by simultaneously fitting for the habitable zone inner edge discontinuity in the subsample without RV follow-up. An optimized mission in search for the inner edge of the habitable zone will further enhance its information content via an informed selection of follow-up targets, i.e., balancing objects located on either side of the expected instellation threshold S_{thresh}.

6.4.2. *The importance of M dwarfs in the target list*

To date, the majority of planets with radius measurements orbit FGK dwarfs, and, based on the instellation they receive, most of them lie in the runaway greenhouse regime (Thompson et al. 2018). Obviously, a radius/density discontinuity in the exoplanet demographics like the habitable zone inner edge discontinuity cannot be constrained well if only one side of the discontinuity is being sampled. This, however, is the situation for planetary systems around Sun-like stars – their habitable zones are so distant that transiting planets within them are very rare due to pure geometrical reasons. It was, among other reasons, the sharp drop in transit probability with orbital distance that has prompted a number of recent transit surveys to specifically target M dwarfs (e.g., Irwin et al. 2009; Obermeier et al. 2016; Delrez et al. 2018; Sebastian et al. 2021; Dietrich et al. 2023), but the sample of terrestrial planets orbiting them is still small (e.g., Berger et al. 2020; Hardegree-Ullman et al. 2020).

M dwarf systems are also key for detecting the runaway greenhouse transition: Our calculations with different spectral types (Sect. 5.4.2) show that the information content of M dwarfs in a sample dominates the hypothesis tests. Besides their large number in a volume/magnitude-limited sample, transiting M dwarf planets are more likely to be located near the threshold instellation and in particular on orbits further out, i.e., in the optimistic habitable zone. In fact, we showed that the FGK part of the planet sample barely contributes to the statistical power. Furthermore, the transit depth difference at the transition is expected to be larger for M dwarfs ($\sim 100\,\mathrm{ppm}$ for early, $\sim 1000\,\mathrm{ppm}$ for late M stars, Turbet et al. 2019), enhancing the demographic signal it leaves. An additional advantage of targeting M dwarfs are the extended runaway greenhouse phases of their planets that can last on the order of gigayears (Luger & Barnes 2015). This increases the probability of observing any given planet in the sample during the runaway greenhouse phase, essentially driving f_{rgh} to higher values. Therefore, in addition to the high scientific value of boosted detections of potentially habitable planets, M dwarfs are also indispensable for the discovery and characterization of the runaway greenhouse transition. As with a pure volume-limited sample, a targeted M dwarf survey, too, profits from follow-up measurements of planetary masses with an order of magnitude increase in evidence.

6.5. *Constraining planetary habitability*

A potential for liquid water on the surface of a planet is commonly used as an environmental marker to assess its surface habitability (Huang 1959; Hart 1978; Kasting et al. 1993; Kaltenegger & Sasselov 2011; Kopparapu et al. 2013). The runaway greenhouse transition represents an upper bound on received irradiation for this condition. Its detection would thus not only empirically confirm the habitable zone concept but also help to locate it in the observationally available planetary parameter space. In Sect. 5.4.3, we show that the threshold instellation at which the runaway greenhouse transition occurs can be reasonably constrained without imposing overly optimistic conditions on the underlying planet population, instrumentation, or survey strategy. A mission like *PLATO* is well equipped to perform this measurement; the constraining power is directly proportional to the proportion of characterized planets around M dwarfs and to the number of planets for which masses can be determined.

The situation is different for the planetary water inventory and the fraction of planets with runaway greenhouse climates: Since these parameters are degenerate, they cannot be well constrained without independent measurements. This degeneracy could be lifted if independent measurements of atmospheric compositions can be made. For example, detections of water vapor in planets above the threshold instellation, combined with precise radius measurements, would constrain the predominant water content of terrestrial planets.

Once a runaway greenhouse region is identified in the parameter space, the community will have a tool at hand to discern potentially habitable planets from Venusian worlds on an empirical basis. Together with atmospheric measurements (see Sect. 6.2.3), we will be able to put a number on the probability of an individual planet to harbor sufficient surface water to sustain life.

6.6. *Impact of assumptions on our findings*

The prospects for probing the runaway greenhouse transition depends on astro- and geophysical factors, as well as on the specific instrumentation and survey strategy of a particular mission. Our state-of-the-art models approximate the situation and offer testable predictions. In the following, we review a few considerations that future models may include to refine these predictions.

6.6.1. *Structures in the planet occurrence rate density*

The baseline occurrence rate density in radius-period space that governs the generation of synthetic planets might influence our findings, especially if it contains any features that coincide with the injected demographic feature. This is not the case in the model from Bergsten et al. (2022) that we adopted: Its occurrence rate density varies smoothly in the domain relevant for the runaway greenhouse hypothesis; transitions only occur at smaller instellations ($< 50\,\mathrm{W\,m^{-2}}$) and larger radii ($> 1.6\,R_\oplus$). We thus do not expect the model underlying our planet sample to affect the investigation of the habitable zone inner edge discontinuity. If any currently unknown sharp features in the distribution of terrestrial planets emerge, they should be considered in future studies.

6.6.2. *Baseline mass-radius relationship*

Our baseline mass-radius relationship assuming pure $MgSiO_3$ interiors (Zeng et al. 2016) might not be representative of the rocky planet population. However, while interior composition may introduce an offset to the radius habitable zone inner edge discontinuity, we do not expect a change of its structure. Since the magnitude of the radius inflation effect is expected to be larger for an Earth-like interior composition with an iron core-silicate mantle structure (Zeng et al. 2016; Noack & Lasbleis 2020; Bonati et al. 2021), we consider our mass-radius relationship a conservative case. We performed a sanity check to assess the impact of varying our baseline model (see Appendix A.3) and found general agreement between different interior compositions.

Future self-consistent modeling of interior-atmosphere interactions may include constraints on additional radius increases due to a molten interior (Bower et al. 2019) and any potential effects stemming from a deviating gas exchange between atmosphere and interior in runaway greenhouse planets due to different redox conditions (Ikoma et al. 2018; Lichtenberg et al. 2021; Bower et al. 2022; Gaillard et al. 2021) or water outgassing efficiency (e.g., Hier-Majumder & Hirschmann 2017; Ikoma et al. 2018; Salvador & Samuel 2023).

6.6.3. *Bulk water mass fraction*

The predominant mass fractions of water, which sensitively controls the atmospheric state of a rocky exoplanet, is poorly constrained. Inferred water contents in the literature range from upper limits on the order 10^{-5} to "water worlds" with tens of percent mass fraction (e.g., Rogers & Seager 2010; Unterborn et al. 2018; Mousis et al. 2020; Agol et al. 2021; Luque & Pallé 2022), all of which are within the realm of theoretical predictions (Selsis et al. 2007; Mulders et al. 2015; Sato et al. 2016; Jin & Mordasini 2018; Lichtenberg et al. 2019; Bitsch et al. 2019; Venturini et al. 2020; Emsenhuber et al. 2021; Schlecker et al. 2021a; Lichtenberg & Clement 2022; Izidoro et al. 2022). Our nominal case assumes a bulk water mass fraction of $x_{\mathrm{H_2O}} = 0.005$. This can be considered a conservative choice that is unlikely to introduce a systematic overestimation of the habitable zone inner edge discontinuity. Cases of pure rocky composition and very low volatile contents can be considered absorbed by the dilution factor f_{rgh}. Assuming a distribution of water mass fractions instead of a fixed value would thus not significantly change our results.

6.6.4. *"Sharpness" of the habitable zone inner edge discontinuity*

The habitable zone inner edge discontinuity may be affected by several processes that are challenging to quantify: Planets that lack an atmosphere, sufficient volatiles, or have non-water-dominated outgassed compositions cannot bear steam atmospheres, and those that do eventually move to the non-runaway greenhouse category due to desiccation (Watson et al. 1981; Kasting & Pollack 1983; Hamano et al. 2013) or evolution of their host star (Luger & Barnes 2015). Hydrogen/Helium-dominated planets may disguise as inflated rocky planets and not contribute to the demographic signal, although a runaway greenhouse radius inflation effect was suggested for water-dominated sub-Neptunes (Pierrehumbert 2022; Innes et al. 2023). A subset of such gas-rich planets will experience atmospheric loss via photoevaporation (Owen & Wu 2013) or core-powered mass loss (Ginzburg et al. 2018), reducing their transit radius. Intrinsic variation in the threshold instellation is caused by differences in planetary features influencing the onset of a runaway climate such as albedo, atmospheric composition, clouds, or surface gravity (Salvador et al. 2017; Turbet et al. 2021; Lichtenberg et al. 2021; Pierrehumbert 2022; Innes et al. 2023). The choice of a statistical estimator for the hypothesis tests may further influence the recovered discontinuity; we compare our nominal running mean approach with a binned statistic in Appendix A.1.

While these factors may offset the signal's amplitude, they preserve its general shape. The "dilution factor" f_{rgh} in our model embodies our ignorance of the magnitude of this offset. In a real survey, additional contextual information about planets in the sample may be available.

7. CONCLUSIONS

Significant inflation of rocky planet radii is a robust prediction of runaway greenhouse models. Using `Bioverse`, a quantitative hypothesis testing framework, we have explored the potential of contemporary exoplanet missions to statistically detect a radius/density discontinuity resulting from this inflation in the exoplanet population. Our key findings are as follows:

1. The predicted runaway greenhouse transition causes a discontinuity in the radius and density

distribution of small exoplanets with respect to their irradiation.

2. This habitable zone inner edge discontinuity should be detectable with high-precision transit measurements. For a planet sample $\gtrsim 100$, a detection is likely if radius inflation occurs on at least 10 % of the observed planets and if typical bulk water mass fractions are above $\sim 10^{-3}$.

3. We find that the planned *PLATO* transit survey will provide a sufficient sample and the required precision to confirm or reject the predicted trend. Assuming the projected photometric precision, *PLATO* will be able to test the runaway greenhouse hypothesis for planet yields $\gtrsim 100$.

4. The diagnostic power of transit missions in testing this hypothesis can be increased through a follow-up campaign providing planet mass measurements. This can reduce the required planet yield by about a factor of three. Only an adequate sample of planets orbiting M dwarfs will ensure sufficient targets on both sides of the expected threshold instellation.

5. Testing the runaway greenhouse hypothesis on a population level can provide constraints on the water inventory of rocky exoplanets and thus make an important contribution to assessing their habitability. A detection will provide an empirical confirmation of the habitable zone concept and localize its inner edge.

The habitable zone concept is widely employed in target prioritization for exoplanet missions, and it will provide context for interpreting potential signatures of life. As we have demonstrated, it appears realistic that an empirical test of the habitable zone hypothesis is imminent. The confirmation or rejection of the habitable zone inner edge discontinuity will be a key contribution to understanding the diversity of exoplanet climates and the search for extraterrestrial life in the Universe.

The authors thank Gabriele Cugno, Yann Fabel, Brad Foley, Lisa Kaltenegger, Ravi Kopparapu, Eric Mamajek, Megan Mansfield, Paul Molliere, Gijs Mulders, Matthew Murphy, Sukrit Ranjan, and Terry-Ann Suer for insightful discussions. We are grateful to Martin Turbet for providing the mass-radius relationship data for planets harboring steam atmospheres. We thank the anonymous referees for providing insightful reports that helped to improve this manuscript. This material is based upon work supported by the National Aeronautics and Space Administration under Agreement No. 80NSSC21K0593 for the program "Alien Earths". The results reported herein benefited from collaborations and/or information exchange within NASA's Nexus for Exoplanet System Science (NExSS) research coordination network sponsored by NASA's Science Mission Directorate. This work has made use of data from the European Space Agency (ESA) mission *Gaia* (https://www.cosmos.esa.int/gaia), processed by the *Gaia* Data Processing and Analysis Consortium (DPAC, https://www.cosmos.esa.int/web/gaia/dpac/consortium). Funding for the DPAC has been provided by national institutions, in particular the institutions participating in the *Gaia* Multilateral Agreement. T.L. was supported by a grant from the Branco Weiss Foundation. G.B. acknowledges support from the NASA Astrophysics Data Analysis Program under Grant No. 80NSSC20K0446. A.S. acknowledges support from NASA's Habitable Worlds Program (No. 80NSSC20K0226).

AUTHOR CONTRIBUTIONS

M.S., D.A., and T.L. conceived the project, planned its implementation, and interpreted the results. D.A. leads the "Alien Earths" program through which this project is funded and helped to guide the strategy of the project. T.L. and A.S. provided expertise on runaway greenhouse climates and exoplanet interiors. M.S. carried out the hypothesis tests and statistical analyses. M.S. wrote the manuscript; T.L., G.B., K.H.-U., and A.S. provided text contributions. G.B. implemented the planet generator in the `Bioverse` framework. All authors provided comments and suggestions on the manuscript.

REPRODUCIBILITY

This study uses the reproducibility framework "showyourwork" (Luger et al. 2021). All code required to reproduce our results, figures, and this article itself is available at https://github.com/matiscke/hz-inner-edge-discontinuity, and the repository state at the time of paper acceptance can be found at doi:10.5281/zenodo.8251077. The code to reproduce a figure can be accessed via the icon link next to the respective figure caption. Data sets associated with this work are available at doi:10.5281/zenodo.7080391 (stellar luminosity tracks from Baraffe et al. (1998)) and doi:10.5281/zenodo.7946446 (results from model grid runs of `Bioverse`).

Software: `Bioverse` (Bixel & Apai 2021), Astropy (Astropy Collaboration et al. 2018), NumPy (Harris et al. 2020), SciPy (Virtanen et al. 2020), corner.py (Foreman-Mackey 2016), dynesty (Speagle 2020).

APPENDIX

A. ROBUSTNESS TESTS

A.1. *Alternative statistics for the average radius or bulk density*

The hypothesis tests introduced in Sect. 4 rely on a statistical estimator for the variation of planetary radii or bulk densities as a function of net instellation, and we chose a moving average for this estimator in our nominal setup. Here, we explore how robust our results are against this choice by demonstrating the recovery of the runaway greenhouse signal in the case of the optimistic survey (Sect. 5.2) with an alternative estimator: instead of computing moving averages, we used a binned statistic.

We first binned the data of the simulated survey in instellation space, choosing the number of bins via the rule of Freedman & Diaconis (1981) and using logarithmic binning. In each bin, we computed the arithmetic mean of the planet radius and its standard deviation. Then, we assigned each planet the mean radius according to the instellation bin it occupies and used this as the measure for testing the runaway greenhouse hypothesis.

Figure 10 shows the simulated data together with binned, average planet radii and draws from the posterior of the hypothesis test. A clear detection resulted, although with somewhat lower significance ($\Delta \ln \mathcal{Z} \approx 30$) compared to the nominal setup. The accuracy of the recovered instellation threshold is comparable. This test demonstrates that our results are not sensitive to the choice of statistical estimator to test the hypotheses against.

It is conceivable that with very large sample sizes and a very sharp runaway greenhouse transition a binned solution would perform better. For a search with real data, both approaches, and possibly other alternatives, should be considered.

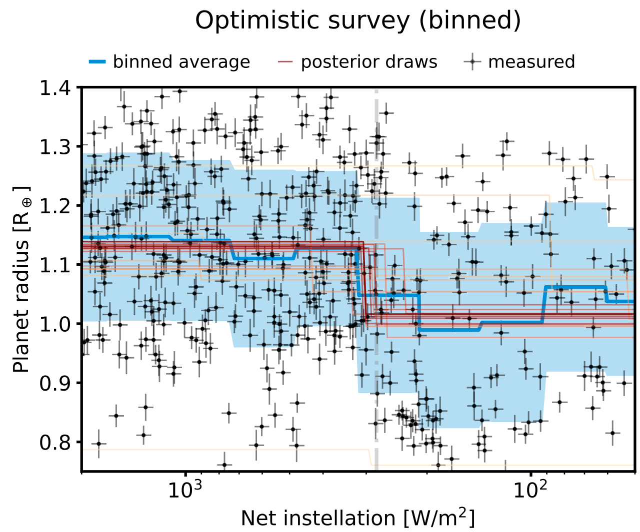

Figure 10. Detection of the runaway greenhouse threshold with a binned statistic. Using simulated data from the optimistic survey case ($N = 500$, compare Figure 5), we tested the runaway greenhouse hypothesis. Instead of using a running mean, we computed a binned statistic (arithmetic mean and standard deviation in blue) to assign planets the average radius or bulk density in their neighborhood in instellation space. Random draws from the posterior of the runaway greenhouse hypothesis (Eqn. 4) are shown in red. As in the nominal case, the pattern is detected with high significance.

A.2. *Statistical imprint of runaway greenhouse atmospheres*

The predicted runaway greenhouse-induced planet radius changes are a function of instellation, planet mass, and bulk water mass fraction (compare Sect. 3). In order to better understand the interaction between the planetary populations underlying our simulations and these predictions, we compared the latter to the average radius and bulk density changes we measured in the synthetic population. We used the "optimistic" scenario with a sample size of 500.

Figure 11 shows this comparison for a range of planetary masses and water mass fractions. The complex dependence of the radius inflation on these parameters is evident, but no significant abrupt changes capable of causing spurious signals occur. Differences between model prediction and population can be explained by the wide dispersion in planet mass in the population.

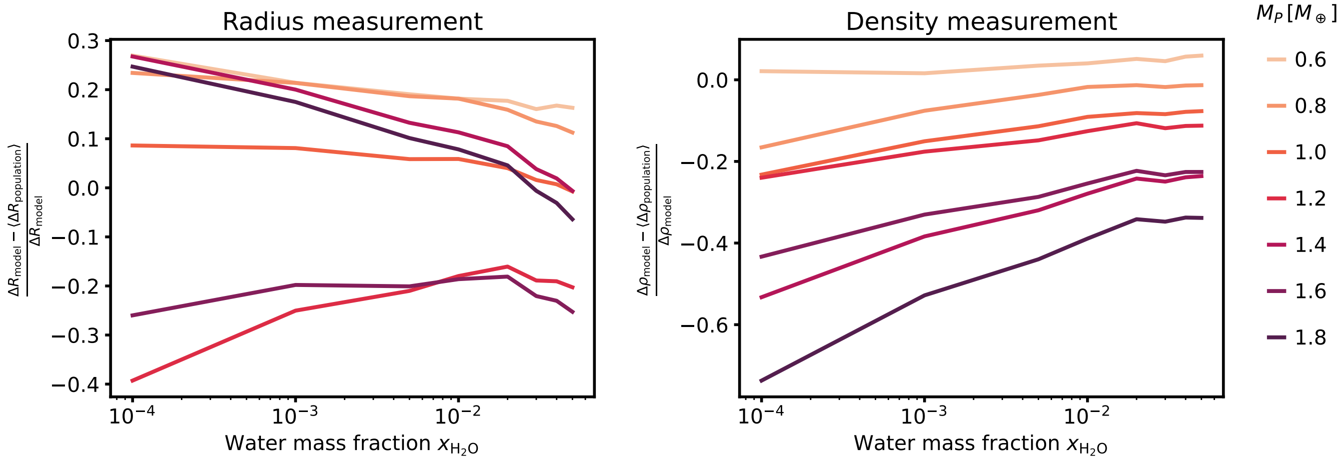

Figure 11. Comparison of radius and bulk density changes predicted by the atmospheric models to the average changes measured in the synthetic planet population. Model predictions $\Delta R_{\mathrm{model}}$ and $\Delta \rho_{\mathrm{model}}$ depend on individual planet masses; $\langle \Delta R_{\mathrm{population}} \rangle$ and $\langle \Delta \rho_{\mathrm{population}} \rangle$ are averaged measurements of the overall population. Significant differences are thus expected.

A.3. *Influence of different mass-radius relationships on our results*

We assessed how a different choice of baseline mass-radius relation influences our results. Focussing on the detectability of the statistical runaway greenhouse signal and the ability to constrain the threshold instellation, we repeated the hypothesis test in Sect. 5.2 with alternative mass-radius relationships. Instead of assuming a pure $\mathrm{MgSiO_3}$ composition, we assigned planet masses using either the probabilistic relationship in Wolfgang et al. (2016) or a semi-empirical, two-layer relation assuming an Earth-like (32.5 % Fe + 67.5 % $\mathrm{MgSiO_3}$) composition (Zeng et al. 2016).

Figure 12 shows how the two alternative baseline mass-radius relations influence the significance of a detection and the ability to constrain the threshold instellation. The relation of Wolfgang et al. (2016) includes intrinsic scatter, which impedes a detection at low dilution factors. In this regime, a layered, Earth-like composition leads to more significant detections and a narrower, although biased, constraint on S_{thresh}. Both mass-radius relations agree and recover the injected value where the null hypothesis can be rejected with high significance. This is consistent with our nominal mass-radius relation (compare Sect. 2.4). We conclude that the underlying core and mantle composition of planets may affect the detectability of the transition if the fraction of planets with runaway greenhouse climates is low; however, the overall trends that our experiments revealed appear robust.

We caution that this analysis may serve only as a sanity check and should not be taken as a result in itself: The atmospheric model from Turbet et al. (2020) we adopted relies on a silicate interior composition for its transit radius prediction. Therefore, only our nominal procedure throughout the main body of the paper represents a self-consistent treatment.

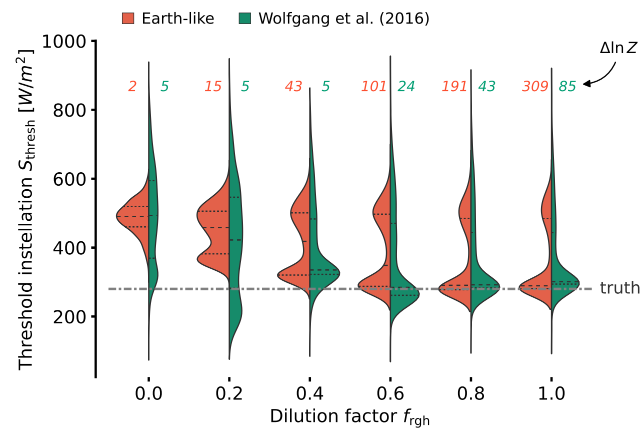

Figure 12. Posterior threshold instellations as a function of dilution factor for two alternative baseline mass-radius relations. For each grid step in f_{rgh}, we show kernel density estimates of retrieved posteriors (averaged over 50 iterations) assuming an Earth-like (32.5 % Fe + 67.5 % $\mathrm{MgSiO_3}$) composition or the probabilistic relation from Wolfgang et al. (2016) and otherwise following the optimistic scenario in Sect. 5.2. Lines within the violins show quartiles of the distributions, and the gray line indicates the injected threshold instellation of $280\,\mathrm{W\,m^{-2}}$. Higher log-evidence differences $\Delta \ln Z$ correspond to more significant rejections of the null hypothesis. In the regime of strong detections, both mass-radius relations lead to similar, accurate constraints on S_{thresh}. Differences occur at low dilution factors, where the Earth-like relation leads to narrower estimates.

REFERENCES

Adams, F. C., Bodenheimer, P., & Laughlin, G. 2005, Astronomische Nachrichten, 326, 913, doi: 10.1002/asna.200510440

Agol, E., Dorn, C., Grimm, S. L., et al. 2021, Planet. Sci. J., 2, 1, doi: 10.3847/PSJ/abd022

Aguichine, A., Mousis, O., Deleuil, M., & Marcq, E. 2021, ApJ, 914, 84, doi: 10.3847/1538-4357/abfa99

Alei, E., Konrad, B. S., Angerhausen, D., et al. 2022, A&A, 665, A106, doi: 10.1051/0004-6361/202243760

Alexander, C. M. O., McKeegan, K. D., & Altwegg, K. 2018, SSRv, 214, 36, doi: 10.1007/s11214-018-0474-9

Angerhausen, D., DeLarme, E., & Morse, J. A. 2015, PASP, 127, 1113, doi: 10.1086/683797

Apai, D., Milster, T. D., Kim, D. W., et al. 2019a, AJ, 158, 83, doi: 10.3847/1538-3881/ab2631

Apai, D., Banzatti, A., Ballering, N. P., et al. 2019b, Bulletin of the AAS, 51

Apai, D., Milster, T. D., Kim, D., et al. 2022, in Optical Manufacturing and Testing XIV, Vol. 12221 (SPIE), 59–71, doi: 10.1117/12.2633184

Astropy Collaboration, Price-Whelan, A. M., Sipőcz, B. M., et al. 2018, The Astronomical Journal, 156, 123, doi: 10.3847/1538-3881/aabc4f

Baraffe, I., Chabrier, G., Allard, F., & Hauschildt, P. H. 1998, Astronomy and Astrophysics, v.337, p.403-412 (1998), 337, 403

Barclay, T., Pepper, J., & Quintana, E. V. 2018, ApJS, 239, 2, doi: 10.3847/1538-4365/aae3e9

Barnes, J. W. 2007, Publications of the Astronomical Society of the Pacific, 119, 986, doi: 10.1086/522039

Barnes, R., Mullins, K., Goldblatt, C., et al. 2013, Astrobiology, 13, 225, doi: 10.1089/ast.2012.0851

Barth, P., Carone, L., Barnes, R., et al. 2021, Astrobiology, 21, 1325, doi: 10.1089/ast.2020.2277

Bean, J. L., Abbot, D. S., & Kempton, E. M.-R. 2017, ApJL, 841, L24, doi: 10.3847/2041-8213/aa738a

Bean, J. L., Raymond, S. N., & Owen, J. E. 2021, Journal of Geophysical Research (Planets), 126, e06639, doi: 10.1029/2020JE006639

Benz, W., Broeg, C., Fortier, A., et al. 2021, Exp Astron, 51, 109, doi: 10.1007/s10686-020-09679-4

Berger, T. A., Huber, D., Gaidos, E., van Saders, J. L., & Weiss, L. M. 2020, The Astronomical Journal, 160, 108, doi: 10.3847/1538-3881/aba18a

Bergsten, G. J., Pascucci, I., Mulders, G. D., Fernandes, R. B., & Koskinen, T. T. 2022, AJ, 164, 190, doi: 10.3847/1538-3881/ac8fea

Bitsch, B., Raymond, S. N., & Izidoro, A. 2019, A&A, 624, A109, doi: 10.1051/0004-6361/201935007

Bixel, A., & Apai, D. 2020, The Astrophysical Journal, 896, 131, doi: 10.3847/1538-4357/ab8fad

—. 2021, The Astronomical Journal, 161, 228, doi: 10.3847/1538-3881/abe042

Bonati, I., Lasbleis, M., & Noack, L. 2021, Journal of Geophysical Research (Planets), 126, e06724, doi: 10.1029/2020JE006724

Bonati, I., Lichtenberg, T., Bower, D. J., Timpe, M. L., & Quanz, S. P. 2019, A&A, 621, A125, doi: 10.1051/0004-6361/201833158

Bonsor, A., Lichtenberg, T., Drążkowska, J., & Buchan, A. M. 2023, Nature Astronomy, 7, 39, doi: 10.1038/s41550-022-01815-8

Boukrouche, R., Lichtenberg, T., & Pierrehumbert, R. T. 2021, ApJ, 919, 130, doi: 10.3847/1538-4357/ac1345

Bower, D. J., Hakim, K., Sossi, P. A., & Sanan, P. 2022, PSJ, 3, 93, doi: 10.3847/PSJ/ac5fb1

Bower, D. J., Kitzmann, D., Wolf, A. S., et al. 2019, A&A, 631, A103, doi: 10.1051/0004-6361/201935710

Brandl, B., Bettonvil, F., van Boekel, R., et al. 2021, The Messenger, 182, 22, doi: 10.18727/0722-6691/5218

Broadley, M. W., Bekaert, D. V., Piani, L., Füri, E., & Marty, B. 2022, Nature, 611, 245, doi: 10.1038/s41586-022-05276-x

Burn, R., Schlecker, M., Mordasini, C., et al. 2021, A&A, 656, A72, doi: 10.1051/0004-6361/202140390

Catling, D. C., & Zahnle, K. J. 2020, Science Advances, 6, eaax1420, doi: 10.1126/sciadv.aax1420

Chabrier, G. 2003, Publications of the Astronomical Society of the Pacific, 115, 763, doi: 10.1086/376392

Chao, K.-H., deGraffenried, R., Lach, M., et al. 2021, Chemie der Erde / Geochemistry, 81, 125735, doi: 10.1016/j.chemer.2020.125735

Chaverot, G., Turbet, M., Bolmont, E., & Leconte, J. 2022, A&A, 658, A40, doi: 10.1051/0004-6361/202142286

Checlair, J., Abbot, D. S., Webber, R. J., et al. 2019, Bulletin of the AAS, 51

Cockell, C., Bush, T., Bryce, C., et al. 2016, Astrobiology, 16, 89, doi: 10.1089/ast.2015.1295

Crass, J., Gaudi, B. S., Leifer, S., et al. 2021, eprint arXiv:2107.14291, arXiv:2107.14291, doi: 10.48550/arXiv.2107.14291

Crow, C. A., McFadden, L. A., Robinson, T., et al. 2011, ApJ, 729, 130, doi: 10.1088/0004-637X/729/2/130

Currie, T., Biller, B., Lagrange, A.-M., et al. 2022, arXiv e-prints, arXiv:2205.05696, doi: 10.48550/arXiv.2205.05696

Cutri, R. M., Skrutskie, M. F., van Dyk, S., et al. 2003, 2MASS All Sky Catalog of point sources.

Dannert, F. A., Ottiger, M., Quanz, S. P., et al. 2022, A&A, 664, A22, doi: 10.1051/0004-6361/202141958

Defrère, D., Léger, A., Absil, O., et al. 2018, Experimental Astronomy, 46, 543, doi: 10.1007/s10686-018-9613-2

Delrez, L., Gillon, M., Queloz, D., et al. 2018, in Ground-Based and Airborne Telescopes VII, Vol. 10700 (SPIE), 446–466, doi: 10.1117/12.2312475

Diamond-Lowe, H., Kreidberg, L., Harman, C. E., et al. 2022, AJ, 164, 172, doi: 10.3847/1538-3881/ac7807

Dietrich, J., Apai, D., Schlecker, M., et al. 2023, EDEN Survey: Small Transiting Planet Detection Limits and Constraints on the Occurrence Rates for Late M Dwarfs within 15 Pc

Donahue, T. M., Hoffman, J. H., Hodges, R. R., & Watson, A. J. 1982, Science, 216, 630, doi: 10.1126/science.216.4546.630

Dorn, C., & Lichtenberg, T. 2021, ApJL, 922, L4, doi: 10.3847/2041-8213/ac33af

Dreizler, S., I., J., et al. 2020, Astronomy & Astrophysics

Dressing, C. D., & Charbonneau, D. 2015, ApJ, 807, 45, doi: 10.1088/0004-637X/807/1/45

Elkins-Tanton, L. T. 2012, Annual Review of Earth and Planetary Sciences, 40, 113, doi: 10.1146/annurev-earth-042711-105503

Elkins-Tanton, L. T., & Seager, S. 2008, ApJ, 685, 1237, doi: 10.1086/591433

Emsenhuber, A., Mordasini, C., Burn, R., et al. 2021, A&A, 656, A70, doi: 10.1051/0004-6361/202038863

ESA. 2017, PLATO DEFINITION STUDY REPORT (RED BOOK), Tech. Rep. ESA-SCI(2017)1, European Space Agency

Essack, Z., Seager, S., & Pajusalu, M. 2020, ApJ, 898, 160, doi: 10.3847/1538-4357/ab9cba

Fauchez, T. J., Turbet, M., Villanueva, G. L., et al. 2019, The Astrophysical Journal, 887, 194, doi: 10.3847/1538-4357/ab5862

Fegley, Bruce, J., Lodders, K., & Jacobson, N. S. 2020, Chemie der Erde / Geochemistry, 80, 125594, doi: 10.1016/j.chemer.2019.125594

Foreman-Mackey, D. 2016, Journal of Open Source Software, 1, 24, doi: 10.21105/joss.00024

Forget, F., & Leconte, J. 2014, Philosophical Transactions of the Royal Society of London Series A, 372, 20130084, doi: 10.1098/rsta.2013.0084

Fortin, M.-A., Gazel, E., Kaltenegger, L., & Holycross, M. E. 2022, MNRAS, 516, 4569, doi: 10.1093/mnras/stac2198

Freedman, D., & Diaconis, P. 1981, Z. Wahrscheinlichkeitstheorie verw Gebiete, 57, 453, doi: 10.1007/BF01025868

Fulton, B. J., & Petigura, E. A. 2018, AJ, 156, 264, doi: 10.3847/1538-3881/aae828

Fulton, B. J., Petigura, E. A., Howard, A. W., et al. 2017, The Astronomical Journal, 154, 109, doi: 10.3847/1538-3881/aa80eb

Gaia Collaboration, Vallenari, A., Brown, A. G. A., et al. 2022a, Gaia Data Release 3: Summary of the Content and Survey Properties, doi: 10.48550/arXiv.2208.00211

Gaia Collaboration, Arenou, F., Babusiaux, C., et al. 2022b, Gaia Data Release 3: Stellar Multiplicity, a Teaser for the Hidden Treasure

Gaidos, E., Claytor, Z., Dungee, R., Ali, A., & Feiden, G. A. 2023, Monthly Notices of the Royal Astronomical Society, stad343, doi: 10.1093/mnras/stad343

Gaillard, F., Bouhifd, M. A., Füri, E., et al. 2021, SSRv, 217, 22, doi: 10.1007/s11214-021-00802-1

Gaudi, S., Seager, S., Mennesson, B., et al. 2020, arXiv e-prints, arXiv:2001.06683

Gillmann, C., Golabek, G. J., Raymond, S. N., et al. 2020, Nature Geoscience, 13, 265, doi: 10.1038/s41561-020-0561-x

Gillon, M., Jehin, E., Lederer, S. M., et al. 2016, Nature, 533, 221, doi: 10.1038/nature17448

Gillon, M., Triaud, A. H., Demory, B. O., et al. 2017, Nature, 542, 456, doi: 10.1038/nature21360

Ginzburg, S., Schlichting, H. E., & Sari, R. 2016, The Astrophysical Journal, 825, 29, doi: 10.3847/0004-637x/825/1/29

—. 2018, Monthly Notices of the Royal Astronomical Society, 476, 759, doi: 10.1093/mnras/sty290

Goldblatt, C. 2015, Astrobiology, 15, 362, doi: 10.1089/ast.2014.1268

Goldblatt, C., Robinson, T. D., Zahnle, K. J., & Crisp, D. 2013, Nature Geosci, 6, 661, doi: 10.1038/ngeo1892

Goldblatt, C., & Watson, A. J. 2012, Philosophical Transactions of the Royal Society A: Mathematical, Physical and Engineering Sciences, 370, 4197, doi: 10.1098/rsta.2012.0004

Graham, R. J., Lichtenberg, T., & Pierrehumbert, R. T. 2022, Journal of Geophysical Research (Planets), 127, e2022JE007456, doi: 10.1029/2022JE007456

Graham, R. J., & Pierrehumbert, R. 2020, ApJ, 896, 115, doi: 10.3847/1538-4357/ab9362

Grenfell, J. L., Leconte, J., Forget, F., et al. 2020, SSRv, 216, 98, doi: 10.1007/s11214-020-00716-4

Grewal, D. S., Seales, J. D., & Dasgupta, R. 2022, Earth and Planetary Science Letters, 598, 117847, doi: 10.1016/j.epsl.2022.117847

Gupta, A., & Schlichting, H. E. 2019, Monthly Notices of the Royal Astronomical Society, 487, 24, doi: 10.1093/mnras/stz1230

Haar, T. H. V., & Suomi, V. E. 1971, Journal of the Atmospheric Sciences, 28, 305, doi: 10.1175/1520-0469(1971)028{$<$}0305:MOTERB{$>$}2.0.CO;2

Hakim, K., Tian, M., Bower, D. J., & Heng, K. 2023, ApJL, 942, L20, doi: 10.3847/2041-8213/aca90c

Hamano, K., Abe, Y., & Genda, H. 2013, Nature, 497, 607, doi: 10.1038/nature12163

Hamano, K., Kawahara, H., Abe, Y., Onishi, M., & Hashimoto, G. L. 2015, ApJ, 806, 216, doi: 10.1088/0004-637X/806/2/216

Hardegree-Ullman, K. K., Apai, D., Bergsten, G. J., Pascucci, I., & López-Morales, M. 2023, Bioverse: A Comprehensive Assessment of the Capabilities of Extremely Large Telescopes to Probe Earth-like O$_\mathrm{2}$ Levels in Nearby Transiting Habitable Zone Exoplanets, arXiv, doi: 10.48550/arXiv.2304.12490

Hardegree-Ullman, K. K., Zink, J. K., Christiansen, J. L., et al. 2020, The Astrophysical Journal Supplement Series, 247, 28, doi: 10.3847/1538-4365/ab7230

Harris, C. R., Millman, K. J., van der Walt, S. J., et al. 2020, Nature, 585, 357, doi: 10.1038/s41586-020-2649-2

Hart, M. H. 1978, Icarus, 33, 23, doi: 10.1016/0019-1035(78)90021-0

Hier-Majumder, S., & Hirschmann, M. M. 2017, Geochemistry, Geophysics, Geosystems, 18, 3078, doi: 10.1002/2017GC006937

Hinkley, S., Vigan, A., Kasper, M., Quanz, S. P., & Lacour, S. 2021, in ExoFrontiers; Big Questions in Exoplanetary Science, ed. N. Madhusudhan, 5–1, doi: 10.1088/2514-3433/abfa8fch5

Hu, R., Damiano, M., Scheucher, M., et al. 2021, ApJL, 921, L8, doi: 10.3847/2041-8213/ac1f92

Huang, S.-S. 1959, American Scientist, 47, 397

Ikoma, M., Elkins-Tanton, L., Hamano, K., & Suckale, J. 2018, Space Science Reviews, 214, 76, doi: 10.1007/s11214-018-0508-3

Ikoma, M., & Hori, Y. 2012, ApJ, 753, 66, doi: 10.1088/0004-637X/753/1/66

Ingersoll, A. P. 1969, Journal of Atmospheric Sciences, 26, 1191, doi: 10.1175/1520-0469(1969)026{$<$}1191:TRGAHO{$>$}2.0.CO;2

Innes, H., Tsai, S.-M., & Pierrehumbert, R. T. 2023, The Runaway Greenhouse Effect on Hycean Worlds, arXiv, doi: 10.48550/arXiv.2304.02698

Irwin, J., Charbonneau, D., Nutzman, P., & Falco, E. 2009, 253, 37, doi: 10.1017/S1743921308026215

Izidoro, A., Schlichting, H. E., Isella, A., et al. 2022, ApJL, 939, L19, doi: 10.3847/2041-8213/ac990d

Jin, S., & Mordasini, C. 2018, The Astrophysical Journal, 853, 163, doi: 10.3847/1538-4357/aa9f1e

Jin, S., Mordasini, C., Parmentier, V., et al. 2014, Astrophysical Journal, 795, doi: 10.1088/0004-637X/795/1/65

Jin, Z., Bose, M., Lichtenberg, T., & Mulders, G. D. 2021, PSJ, 2, 244, doi: 10.3847/PSJ/ac3d86

Johnson, J. A., Howard, A. W., Marcy, G. W., et al. 2010, PASP, 122, 149, doi: 10.1086/651007

Johnstone, C. P. 2020, The Astrophysical Journal, 890, 79, doi: 10.3847/1538-4357/ab6224

Jontof-Hutter, D. 2019, Annual Review of Earth and Planetary Sciences, 47, 141, doi: 10.1146/annurev-earth-053018-060352

Kaltenegger, L., & Sasselov, D. 2011, The Astrophysical Journal, 736, L25, doi: 10.1088/2041-8205/736/2/L25

Kane, S. R., Kopparapu, R. K., & Domagal-Goldman, S. D. 2014, ApJL, 794, L5, doi: 10.1088/2041-8205/794/1/L5

Kane, S. R., Arney, G., Crisp, D., et al. 2019, Journal of Geophysical Research (Planets), 124, 2015, doi: 10.1029/2019JE005939

Kane, S. R., Arney, G. N., Byrne, P. K., et al. 2021, Journal of Geophysical Research (Planets), 126, e06643, doi: 10.1029/2020JE006643

Kasting, J. F. 1988, Icarus, 74, 472, doi: 10.1016/0019-1035(88)90116-9

Kasting, J. F., & Pollack, J. B. 1983, Icarus, 53, 479, doi: 10.1016/0019-1035(83)90212-9

Kasting, J. F., Whitmire, D. P., & Reynolds, R. T. 1993, Icarus, 101, 108, doi: 10.1006/icar.1993.1010

Katyal, N., Nikolaou, A., Godolt, M., et al. 2019, ApJ, 875, 31, doi: 10.3847/1538-4357/ab0d85

Kimura, T., & Ikoma, M. 2020, MNRAS, 496, 3755, doi: 10.1093/mnras/staa1778

—. 2022, Nature Astronomy, 6, 1296, doi: 10.1038/s41550-022-01781-1

Kipping, D. M. 2013, Monthly Notices of the Royal Astronomical Society: Letters, 434, L51, doi: 10.1093/mnrasl/slt075

Kite, E. S., & Schaefer, L. 2021, ApJL, 909, L22, doi: 10.3847/2041-8213/abe7dc

Kleine, T., Budde, G., Burkhardt, C., et al. 2020, SSRv, 216, 55, doi: 10.1007/s11214-020-00675-w

Koll, D. D. B., Malik, M., Mansfield, M., et al. 2019, ApJ, 886, 140, doi: 10.3847/1538-4357/ab4c91

Konrad, B. S., Alei, E., Quanz, S. P., et al. 2022, A&A, 664, A23, doi: 10.1051/0004-6361/202141964

Kopparapu, R. K., Ramirez, R. M., SchottelKotte, J., et al. 2014, ApJL, 787, L29, doi: 10.1088/2041-8205/787/2/L29

Kopparapu, R. K., Ramirez, R., Kasting, J. F., et al. 2013, ApJ, 765, 131, doi: 10.1088/0004-637X/765/2/131

Krijt, S., Kama, M., McClure, M., et al. 2022, Chemical Habitability: Supply and Retention of Life's Essential Elements During Planet Formation

Krissansen-Totton, J., Fortney, J. J., & Nimmo, F. 2021, Planet. Sci. J., 2, 216, doi: 10.3847/PSJ/ac2580

Leconte, J., Forget, F., Charnay, B., Wordsworth, R., & Pottier, A. 2013a, Nature, 504, 268, doi: 10.1038/nature12827

Leconte, J., Forget, F., Charnay, B., et al. 2013b, A&A, 554, A69, doi: 10.1051/0004-6361/201321042

Leconte, J., Forget, F., & Lammer, H. 2015, Experimental Astronomy, 40, 449, doi: 10.1007/s10686-014-9403-4

Lehmer, O. R., Catling, D. C., & Krissansen-Totton, J. 2020, Nat Commun, 11, 6153, doi: 10.1038/s41467-020-19896-2

Lichtenberg, T. 2021, ApJL, 914, L4, doi: 10.3847/2041-8213/ac0146

Lichtenberg, T., Bower, D. J., Hammond, M., et al. 2021, Journal of Geophysical Research: Planets, 126, e2020JE006711, doi: 10.1029/2020JE006711

Lichtenberg, T., Bower, D. J., Hammond, M., et al. 2021a, Journal of Geophysical Research (Planets), 126, e06711, doi: 10.1029/2020JE006711

Lichtenberg, T., & Clement, M. S. 2022, ApJL, 938, L3, doi: 10.3847/2041-8213/ac9521

Lichtenberg, T., Drążkowska, J., Schönbächler, M., Golabek, G. J., & Hands, T. O. 2021b, Science, 371, 365, doi: 10.1126/science.abb3091

Lichtenberg, T., Golabek, G. J., Burn, R., et al. 2019, Nat Astron, 3, 307, doi: 10.1038/s41550-018-0688-5

Lichtenberg, T., & Krijt, S. 2021, ApJL, 913, L20, doi: 10.3847/2041-8213/abfdce

Lichtenberg, T., Schaefer, L. K., Nakajima, M., & Fischer, R. A. 2022, Geophysical Evolution During Rocky Planet Formation

Lincowski, A. P., Lustig-Yaeger, J., & Meadows, V. S. 2019, AJ, 158, 26, doi: 10.3847/1538-3881/ab2385

Liu, B., Raymond, S. N., & Jacobson, S. A. 2022, Nature, 604, 643, doi: 10.1038/s41586-022-04535-1

Loftus, K., Wordsworth, R. D., & Morley, C. V. 2019, ApJ, 887, 231, doi: 10.3847/1538-4357/ab58cc

Luger, R., & Barnes, R. 2015, Astrobiology, 15, 119, doi: 10.1089/ast.2014.1231

Luger, R., Bedell, M., Foreman-Mackey, D., et al. 2021, Mapping Stellar Surfaces III: An Efficient, Scalable, and Open-Source Doppler Imaging Model

Luger, R., Sestovic, M., Kruse, E., et al. 2017, Nature Astronomy, 1, 1, doi: 10.1038/s41550-017-0129

Lupu, R. E., Zahnle, K., Marley, M. S., et al. 2014, ApJ, 784, 27, doi: 10.1088/0004-637X/784/1/27

Luque, R., & Pallé, E. 2022, Science, 377, 1211, doi: 10.1126/science.abl7164

Lustig-Yaeger, J., Meadows, V. S., Tovar Mendoza, G., et al. 2018, The Astronomical Journal, 156, 301, doi: 10.3847/1538-3881/aaed3a

Mann, A. W., Feiden, G. A., Gaidos, E., Boyajian, T., & von Braun, K. 2015, ApJ, 804, 64, doi: 10.1088/0004-637X/804/1/64

Mann, A. W., Dupuy, T., Kraus, A. L., et al. 2019, ApJ, 871, 63, doi: 10.3847/1538-4357/aaf3bc

Mansfield, M., Kite, E. S., Hu, R., et al. 2019, ApJ, 886, 141, doi: 10.3847/1538-4357/ab4c90

Marcantonio, P. D., Zanutta, A., Marconi, A., et al. 2022, in Modeling, Systems Engineering, and Project Management for Astronomy X, Vol. 12187 (SPIE), 9–23, doi: 10.1117/12.2628914

Matuszewski, F., Nettelmann, N., Cabrera, J., Börner, A., & Rauer, H. 2023, Estimating the Number of Planets That PLATO Can Detect, arXiv, doi: precision

Mawet, D., Fitzgerald, M., Konopacky, Q., et al. 2019, 51, 134, doi: 10.48550/arXiv.1908.03623

Mazeh, T., Holczer, T., & Faigler, S. 2016, Astronomy and Astrophysics, 589, doi: 10.1051/0004-6361/201528065

McCubbin, F. M., & Barnes, J. J. 2019, Earth and Planetary Science Letters, 526, 115771, doi: 10.1016/j.epsl.2019.115771

Ment, K., & Charbonneau, D. 2023, The Occurrence Rate of Terrestrial Planets Orbiting Nearby Mid-to-late M Dwarfs from TESS Sectors 1-42, doi: 10.48550/arXiv.2302.04242

Mezger, K., Schönbächler, M., & Bouvier, A. 2020, SSRv, 216, 27, doi: 10.1007/s11214-020-00649-y

Miguel, Y., Cridland, A., Ormel, C. W., Fortney, J. J., & Ida, S. 2020, Monthly Notices of the Royal Astronomical Society, 491, 1998, doi: 10.1093/mnras/stz3007

Milster, T. D., Sik Kim, Y., Wang, Z., & Purvin, K. 2020, Applied Optics, 59, 7900, doi: 10.1364/AO.394124

Mollière, P., & Snellen, I. A. G. 2019, A&A, 622, A139, doi: 10.1051/0004-6361/201834169

Montet, B. T., Yee, J. C., & Penny, M. T. 2017, PASP, 129, 044401, doi: 10.1088/1538-3873/aa57fb

Moore, W. B., Lenardic, A., Jellinek, A. M., et al. 2017, Nat Astron, 1, 1, doi: 10.1038/s41550-017-0043

Mordasini, C. 2020, Astronomy and Astrophysics, 638, 1, doi: 10.1051/0004-6361/201935541

Mousis, O., Deleuil, M., Aguichine, A., et al. 2020, ApJL, 896, L22, doi: 10.3847/2041-8213/ab9530

Mulders, G. D., Ciesla, F. J., Min, M., & Pascucci, I. 2015, The Astrophysical Journal, 807, 9, doi: 10.1088/0004-637X/807/1/9

Nakajima, S., Hayashi, Y.-Y., & Abe, Y. 1992, Journal of the Atmospheric Sciences, 49, 2256, doi: 10.1175/1520-0469(1992)049{$<$}2256:ASOTGE{$>$}2.0.CO;2

Nascimbeni, V., Piotto, G., Börner, A., et al. 2022, A&A, 658, A31, doi: 10.1051/0004-6361/202142256

Newton, 1642-1727, I. 1687, Newton's Principia : The Mathematical Principles of Natural Philosophy (First American edition, carefully revised and corrected / with a life of the author, by N. W. Chittenden. New-York : Daniel Adee, 1846.)

Noack, L., & Lasbleis, M. 2020, Astronomy and Astrophysics, 638, A129, doi: 10.1051/0004-6361/202037723

Obermeier, C., Koppenhoefer, J., Saglia, R. P., et al. 2016, Astronomy & Astrophysics, 587, A49, doi: 10.1051/0004-6361/201527633

Owen, J. E., & Wu, Y. 2013, Astrophysical Journal, 775, 1, doi: 10.1088/0004-637X/775/2/105

Owen, J. E., & Wu, Y. 2016, ApJ, 817, 107, doi: 10.3847/0004-637X/817/2/107

Parmentier, V., & Crossfield, I. J. M. 2018, Handbook of Exoplanets, 1419, doi: 10.1007/978-3-319-55333-7_116

Pascucci, I., Mulders, G. D., & Lopez, E. 2019, ApJL, 883, L15, doi: 10.3847/2041-8213/ab3dac

Pecaut, M. J., & Mamajek, E. E. 2013, ApJS, 208, 9, doi: 10.1088/0067-0049/208/1/9

Pepe, F. A., Cristiani, S., Rebolo Lopez, R., et al. 2010, 7735, 77350F, doi: 10.1117/12.857122

Piani, L., Marrocchi, Y., Rigaudier, T., et al. 2020, Science, 369, 1110, doi: 10.1126/science.aba1948

Piaulet, C., Benneke, B., Almenara, J. M., et al. 2022, Nature Astronomy, doi: 10.1038/s41550-022-01835-4

Pierrehumbert, R., & Gaidos, E. 2011, ApJL, 734, L13, doi: 10.1088/2041-8205/734/1/L13

Pierrehumbert, R. T. 2010, Principles of Planetary Climate

Pierrehumbert, R. T. 2022, The Runaway Greenhouse on subNeptune Waterworlds

Pluriel, W., Marcq, E., & Turbet, M. 2019, Icarus, 317, 583, doi: 10.1016/j.icarus.2018.08.023

Prusti, T., de Bruijne, J. H. J., Brown, A. G. A., et al. 2016, A&A, 595, A1, doi: 10.1051/0004-6361/201629272

Puig, L., Pilbratt, G. L., Heske, A., Sanz, I. E., & Crouzet, P.-E. 2016, in Space Telescopes and Instrumentation 2016: Optical, Infrared, and Millimeter Wave, Vol. 9904 (SPIE), 649–657, doi: 10.1117/12.2230964

Quanz, S. P., Absil, O., Benz, W., et al. 2021, Experimental Astronomy, doi: 10.1007/s10686-021-09791-z

Quanz, S. P., Ottiger, M., Fontanet, E., et al. 2022, A&A, 664, A21, doi: 10.1051/0004-6361/202140366

Queloz, D., Mayor, M., Udry, S., et al. 2001, The Messenger, 105, 1

Ramirez, R. M. 2018, Geosciences, 8, 280, doi: 10.3390/geosciences8080280

Ramirez, R. M., & Kaltenegger, L. 2017, ApJL, 837, L4, doi: 10.3847/2041-8213/aa60c8

—. 2018, ApJ, 858, 72, doi: 10.3847/1538-4357/aab8fa

Rauer, H. 2021, PLATO Science Objectives and PLATO Mission Consortium, doi: 10.5281/zenodo.5585341

Rauer, H., Aerts, C., Cabrera, J., & PLATO Team. 2016, Astronomische Nachrichten, 337, 961, doi: 10.1002/asna.201612408

Raymond, S. N., Izidoro, A., & Morbidelli, A. 2020, in Planetary Astrobiology, ed. V. S. Meadows, G. N. Arney, B. E. Schmidt, & D. J. Des Marais, 287, doi: 10.2458/azu_uapress_9780816540068

Raymond, S. N., Quinn, T., & Lunine, J. I. 2004, Icarus, 168, 1, doi: 10.1016/j.icarus.2003.11.019

—. 2006, Icarus, 183, 265, doi: 10.1016/j.icarus.2006.03.011

—. 2007, Astrobiology, 7, 66, doi: 10.1089/ast.2006.06-0126

Reid, I. N., Turner, E. L., Turnbull, M. C., Mountain, M., & Valenti, J. A. 2007, ApJ, 665, 767, doi: 10.1086/519001

Ribas, I., Reiners, A., Zechmeister, M., et al. 2023, The CARMENES Search for Exoplanets around M Dwarfs. Guaranteed Time Observations Data Release 1 (2016-2020)

Ricker, G. R., Winn, J. N., Vanderspek, R., et al. 2014, Journal of Astronomical Telescopes, Instruments, and Systems, 1, 014003, doi: 10.1117/1.JATIS.1.1.014003

Rieke, G. H., Wright, G. S., Böker, T., et al. 2015, PASP, 127, 584, doi: 10.1086/682252

Robinson, T. D., Meadows, V. S., & Crisp, D. 2010, ApJL, 721, L67, doi: 10.1088/2041-8205/721/1/L67

Rogers, L. A., & Seager, S. 2010, ApJ, 712, 974, doi: 10.1088/0004-637X/712/2/974

Salvador, A., Massol, H., Davaille, A., et al. 2017, Journal of Geophysical Research (Planets), 122, 1458, doi: 10.1002/2017JE005286

Salvador, A., Massol, H., Davaille, A., et al. 2017, Journal of Geophysical Research: Planets, 122, 1458, doi: 10.1002/2017JE005286

Salvador, A., & Samuel, H. 2023, Icarus, 390, 115265, doi: 10.1016/j.icarus.2022.115265

Salvador, A., Avice, G., Breuer, D., et al. 2023, Space Science Reviews

Sato, T., Okuzumi, S., & Ida, S. 2016, A&A, 589, A15, doi: 10.1051/0004-6361/201527069

Schaefer, L., & Elkins-Tanton, L. T. 2018, Philosophical Transactions of the Royal Society of London Series A, 376, 20180109, doi: 10.1098/rsta.2018.0109

Schaefer, L., Wordsworth, R. D., Berta-Thompson, Z., & Sasselov, D. 2016, ApJ, 829, 63, doi: 10.3847/0004-637X/829/2/63

Schlecker, M., Mordasini, C., Emsenhuber, A., et al. 2021a, A&A, 656, A71, doi: 10.1051/0004-6361/202038554

Schlecker, M., Pham, D., Burn, R., et al. 2021b, A&A, 656, A73, doi: 10.1051/0004-6361/202140551

Schlecker, M., Burn, R., Sabotta, S., et al. 2022, A&A, 664, A180, doi: 10.1051/0004-6361/202142543

Schlichting, H. E., & Young, E. D. 2022, PSJ, 3, 127, doi: 10.3847/PSJ/ac68e6

Sebastian, D., Gillon, M., Ducrot, E., et al. 2021, A&A, 645, A100, doi: 10.1051/0004-6361/202038827

Selsis, F., Leconte, J., Turbet, M., Chaverot, G., & Bolmont, É. 2023, Nature, 620, 287, doi: 10.1038/s41586-023-06258-3

Selsis, F., Chazelas, B., Bordé, P., et al. 2007, Icarus, 191, 453, doi: 10.1016/j.icarus.2007.04.010

Shapley, H., ed. 1953, Climatic Change: Evidence, Causes, and Effects (Cambridge, MA: Harvard University Press)

Skilling, J. 2004, AIP Conference Proceedings, 735, 395, doi: 10.1063/1.1835238

Smart, R. L., Sarro, L. M., Rybizki, J., et al. 2021, A&A, 649, A6, doi: 10.1051/0004-6361/202039498

Smrekar, S. E., Davaille, A., & Sotin, C. 2018, Space Sci Rev, 214, 88, doi: 10.1007/s11214-018-0518-1

Speagle, J. S. 2020, Monthly Notices of the Royal Astronomical Society, doi: 10.1093/mnras/staa278

Spergel, D., Gehrels, N., Baltay, C., et al. 2015, Wide-Field InfrarRed Survey Telescope-Astrophysics Focused Telescope Assets WFIRST-AFTA 2015 Report, doi: 10.48550/arXiv.1503.03757

Suissa, G., Mandell, A. M., Wolf, E. T., et al. 2020, ApJ, 891, 58, doi: 10.3847/1538-4357/ab72f9

Szabó, G. M., & Kiss, L. L. 2011, Astrophysical Journal Letters, 727, 2, doi: 10.1088/2041-8205/727/2/L44

Szentgyorgyi, A., Baldwin, D., Barnes, S., et al. 2016, in Ground-Based and Airborne Instrumentation for Astronomy VI, Vol. 9908 (SPIE), 657–675, doi: 10.1117/12.2233506

Tamburo, P., Muirhead, P. S., & Dressing, C. D. 2023, Predicting the Yield of Small Transiting Exoplanets around Mid-M and Ultra-Cool Dwarfs in the Nancy Grace Roman Space Telescope Galactic Bulge Time Domain Survey, doi: 10.48550/arXiv.2303.09959

The LUVOIR Team. 2019, arXiv e-prints, arXiv:1912.06219

Thompson, S. E., Coughlin, J. L., Hoffman, K., et al. 2018, ApJS, 235, 38, doi: 10.3847/1538-4365/aab4f9

Torres, G., Andersen, J., & Giménez, A. 2010, A&A Rv, 18, 67, doi: 10.1007/s00159-009-0025-1

Tsai, S.-M., Innes, H., Lichtenberg, T., et al. 2021, ApJL, 922, L27, doi: 10.3847/2041-8213/ac399a

Tuchow, N. W., & Wright, J. T. 2023, ApJ, 944, 71, doi: 10.3847/1538-4357/acb054

Turbet, M., Bolmont, E., Chaverot, G., et al. 2021, Nature, 598, 276, doi: 10.1038/s41586-021-03873-w

Turbet, M., Bolmont, E., Ehrenreich, D., et al. 2020, Astronomy & Astrophysics, Volume 638, id.A41, 638, A41, doi: 10.1051/0004-6361/201937151

Turbet, M., Ehrenreich, D., Lovis, C., Bolmont, E., & Fauchez, T. 2019, A&A, 628, A12, doi: 10.1051/0004-6361/201935585

Unterborn, C. T., Hinkel, N. R., & Desch, S. J. 2018, Res. Notes AAS, 2, 116, doi: 10.3847/2515-5172/aacf43

Van Eylen, V., Agentoft, C., Lundkvist, M. S., et al. 2018, Monthly Notices of the Royal Astronomical Society, 479, 4786, doi: 10.1093/mnras/sty1783

Venturini, J., Guilera, O. M., Haldemann, J., Ronco, M. P., & Mordasini, C. 2020, Astronomy & Astrophysics, 643, L1, doi: 10.1051/0004-6361/202039141

Virtanen, P., Gommers, R., Oliphant, T. E., et al. 2020, Nat Methods, 17, 261, doi: 10.1038/s41592-019-0686-2

Warren, A. O., & Kite, E. S. 2023, Proceedings of the National Academy of Science, 120, e2209751120, doi: 10.1073/pnas.2209751120

Watson, A. J., Donahue, T. M., & Walker, J. C. G. 1981, Icarus, 48, 150, doi: 10.1016/0019-1035(81)90101-9

Way, M. J., & Del Genio, A. D. 2020, Journal of Geophysical Research: Planets, 125, e2019JE006276, doi: 10.1029/2019JE006276

Way, M. J., Del Genio, A. D., Kiang, N. Y., et al. 2016, Geophysical Research Letters, 43, 8376, doi: 10.1002/2016GL069790

Whewell, W. 1858, The Plurality of Worlds

Williams, D. M., & Gaidos, E. 2008, Icarus, 195, 927, doi: 10.1016/j.icarus.2008.01.002

Wolf, E. T., & Toon, O. B. 2015, Journal of Geophysical Research: Atmospheres, 120, 5775, doi: 10.1002/2015JD023302

Wolfgang, A., Rogers, L. A., & Ford, E. B. 2016, ApJ, 825, 19, doi: 10.3847/0004-637X/825/1/19

Wordsworth, R., & Kreidberg, L. 2022, Annual Review of Astronomy and Astrophysics, 60, 159, doi: 10.1146/annurev-astro-052920-125632

Wordsworth, R., & Pierrehumbert, R. 2014, ApJL, 785, L20, doi: 10.1088/2041-8205/785/2/L20

Wordsworth, R. D., & Pierrehumbert, R. T. 2013, ApJ, 778, 154, doi: 10.1088/0004-637X/778/2/154

Wordsworth, R. D., Schaefer, L. K., & Fischer, R. A. 2018, AJ, 155, 195, doi: 10.3847/1538-3881/aab608

Youdin, A. N. 2011, Astrophysical Journal, 742, doi: 10.1088/0004-637X/742/1/38

Yu, X., Moses, J. I., Fortney, J. J., & Zhang, X. 2021, ApJ, 914, 38, doi: 10.3847/1538-4357/abfdc7

Zahnle, K. J., & Carlson, R. W. 2020, in Planetary Astrobiology, ed. V. S. Meadows, G. N. Arney, B. E. Schmidt, & D. J. Des Marais, 3–36, doi: 10.2458/azu_uapress_9780816540068

Zawadzki, B., Carrera, D., & Ford, E. B. 2021, Monthly Notices of the Royal Astronomical Society, 503, 1390, doi: 10.1093/mnras/stab603

Zeng, L., Sasselov, D. D., & Jacobsen, S. B. 2016, ApJ, 819, 127, doi: 10.3847/0004-637X/819/2/127

Zeng, L., Jacobsen, S. B., Sasselov, D. D., et al. 2019, Proceedings of the National Academy of Science, 116, 9723, doi: 10.1073/pnas.1812905116